

ULRR

Report on the pre-test simulation of birdstrike against commuter composite/metal hybrid wing leading edge

Item Type	Report
Authors	McCarthy, Michael A.;Xiao, J. R
Publisher	University of Limerick
Download date	2026-06-09 09:26:49
Item License	https://creativecommons.org/licenses/by-nc-sa/1.0/
Link to Item	https://hdl.handle.net/10344/5072



*DG XII Competitive and Sustainable Growth
Key Action 4: New Perspectives in Aeronautics*



CRAHVI

CRASHWORTHINESS OF AIRCRAFT FOR HIGH VELOCITY IMPACT

Contract N°: G4RD-CT-2000-00395

Proposal N°: GRD1-2000-25242

Deliverable No: D2.2.4

Report on The Pre-test Simulation of Birdstrike against Commuter Composite/Metal Hybrid Wing Leading Edge

M A McCarthy J R Xiao

*Department of Mechanical & Aeronautical Engineering
University of Limerick
Limerick
Republic of Ireland*



University of Limerick

CONTENTS

	Page
Distribution List	3
1 Introduction	4
2 Glare Material Calibration	4
2.1 Available Material Data	4
2.2 Calibration Approach	5
2.3 Material Calibration I: Quasi-static loading	5
2.3.1 Ply Data for aluminium alloy 2024 T3 layers	6
2.3.2 Calibration of Glass Composite Layers	6
2.3.2.1 Global Ply Model Theory	6
2.3.2.2 Glass Composite Calibration Parameters	10
2.3.3 Glare quasi-static 45° test models	18
2.3.4 Glare quasi-static 0° test models	19
2.4 Material Calibration II: High strain rate effects	20
2.4.1 PAM-CRASH strain rate modelling theory	21
2.4.2 High Strain Rate Calibration Parameters	23
3 Bird Strike Models	32
3.1 Bird strike tests to be modelled	32
3.2 Finite element model details	32
3.2.1 FE Meshes	34
3.2.2 Rivet Modelling	36
3.2.3 Boundary Conditions and Contact Interfaces	37
3.2.4 Incorporation of Bird Model	39
3.2.5 Material Models	39
4 Results and Discussion	42
5 Conclusions	66
6 References	66

Distribution List

CRAHVI – European Partners

Mr J. M. Hernandez	European Commission
Dr M. Al-Khalil	Airbus UK Ltd
Dr J. Wiggeraad	NLR
Dr M. A. McCarthy	University of Limerick
Dr D. Hachenberg	Airbus Deutschland
Mr E. Deletombe	ONERA/IMFL
Dr R. Hashemi	Cranfield Impact Centre Ltd
Mr M. Linke	Aachen Technical University
Mr B. Malherbe	Airbus France
Dr A. Kamoulakos	ESI
Prof. T. Kermanidis	University of Patras
Dr N. Petrinic	University of Oxford
Mr F. Arnaudeau	MECALOG
Mr C. Kindervater	DLR
Dr R. Mines	University of Liverpool
Dr W. Rust	CAD-FEM GmbH
Mr B. Reid	DEVTEC
Dr F. Martinez	Principia S.A.
Dr H. C. Manez	EADS – CASA
Mr. V. Melito	Alenia
Mr J. P. Gallard	CEAT



1 Introduction

In sub-task 2.2 of the European Union research Programme “CRAHVI”, the University of Limerick (ULIM) is to perform simulations of birdstrike against structures representative of the leading edge of a commuter aircraft. The skin of these structures is made from a metal/composite hybrid material (Glare). The inputs to this task were test results on Glare under different strain rates from UOXF (D1.1.8) [1], a SPH Bird model created by ESI (D1.4.2) [2], and the geometry of the commuter leading edge structure (in the form of an MSC.Patran file) provided by ALA (D2.1.3) [3]. Some limited background data on Glare was also provided by ALA (D1.1.4) [4]. From these inputs, a mesh has been created and used for pre-test simulation of the birdstrike against the commuter leading edge. Preliminary material calibrations of Glare have also been developed based on the limited data available, with unavailable data provided by reasonable estimation.

This report describes the preliminary material calibrations of Glare, finite element modelling of the LE structure and results of pre-test simulations of forthcoming bird strike tests.

2 Glare Material Calibration

Glare, or Fibre Metal Laminate (FML), is a form of laminated composite material in which a ductile aluminium alloy is combined with a quasi-brittle glass fibre reinforced polymer. Such an assembly is expected to provide a lightweight structure with a greater ability to withstand impact loading at high strain rates than polymer composites or even monolithic aluminium alloys [5]. Two different Glare lay-ups will be used in the skin of the LE structures, produced by ALA, for the birdstrike tests in WP 5:

- FML3 4/3 – 0.4 Total thickness = 2.35 mm with lay-up (A/0/90/A/0/90/A/90/0/A)
- FML5 3/2 – 0.4 Total thickness = 2.20 mm with lay-up (A/0/90/0/90/A/90/0/90/0/A)

where A denotes a layer of aluminium alloy and 0, 90 denote layers of fibrous composite. The metal material used is aluminium alloy 2024 T3 and the composite is glass/epoxy (FM 94-27% - S2 Glass –187 – 460).

2.1 Available Material Data

Material properties of Glare tested in the 0°, 45° and 90° directions under tensile loading at three different strain rates were available from a report by UOXF (D.1.1.8) [1]. Some very limited background data on Glare was also provided by ALA (D1.1.4) [4]. The major difficulty encountered in calibrating a material model for Glare was the extremely limited data available on the constituent materials, particularly the UD S2 glass composite. The data provided by ALA in D2.1.3 [3] on the constituent materials is given in Table 2.1. As can be seen, for the glass composite material, only elastic moduli were available. A search of the literature has so far only yielded stress-strain properties for E-glass (which is quite different from S2 glass). Therefore the properties of the glass layers in the Glare have had to be

estimated using reasonable assumptions. If further data on S2 glass becomes available the calibrations will be updated for the post-test simulation report.

Table 2.1 Mechanical Properties of Metal and Glass Materials used in Glare (from D2.1.3 [3])

Material	Dir'n	E_t	E_c	σ_t	σ_c
		N/mm ²	N/mm ²	N/mm ²	N/mm ²
2024-T3	L	72397,5	73776,5	324,1	-268,9
h = 0.4 mm	LT	72398,0	73777,0	290,0	-310,3
UD Glass	L	53980,0	53980,0	--	--
h = 0.125 mm	LT	9412,0	9412,0	--	--

For aluminium alloy 2024 T3, data was obtained from personal communication with ESI. The stress-strain relationship is defined by a power law as:

$$\sigma(\varepsilon) = a + b(\varepsilon_p)^n \quad (2.1)$$

where a is the yield stress, and b and n are parameters. From ESI's data, $a = 277\text{MPa}$, $b = 485\text{MPa}$ and $n = 0.55$. The Young's modulus was given as 70GPa in ESI's data. ESI's data has been used in this report with Young's modulus changed from 70GPa to 72.4GPa to conform to the information in Table 2.1.

2.2 Calibration Approach

From the UOXF test results on Glare, it can be seen that increasing the strain rate from quasi-static to 3300s^{-1} resulted in a greatly increased ultimate strength and strain in the 0° direction. On the other hand, only minor effects were noticeable on the ultimate strength in the 45° direction (although ultimate strain *was* affected). Since the metal layers should behave more or less the same in both directions, we concluded that the primary cause of the rate dependency in Glare was the S2 glass layers. This conclusion is consistent with observations on Glare in [5]. This report cites several previous studies that concluded that strain rate effects were highly significant in glass/epoxy (in one study, the tensile strength in the fibre direction increased by 116% on increasing the strain rate from quasi-static to 870s^{-1}). On the other hand, several studies were also cited that indicated that the strain rate dependency of the aluminium alloys used in Glare (including 2024 T3), was minor.

2.3 Material Calibration I: Quasi-static loading

This section deals with the calibration of the Glare model in PAM-CRASH for *quasi-static* loading. Rate effects are dealt with in a later section. Multi-layered shell elements with Material Type 131, which is suitable for layered composites, has been used for modelling Glare. Ply TYPE 2 (isotropic, elastic-plastic damaging ply model) is used for the aluminium alloy layers, with no strain rate effects included. Following the above conclusion that strain rate effects in Glare were due primarily to the glass layers, only a ply model with rate effects capability could be used. This ruled out the use of Ply TYPE 0 (Bi-Phase model), which had



been used in CRASURV. Instead Ply TYPE 1 (unidirectional composite global ply model) had to be used.

2.3.1 Ply Data for aluminium alloy 2024 T3 layers

For the aluminium alloy layers, Ply TYPE 2 was used. As noted in Section 2.1, the data from ESI with modified elastic modulus were used. The data cards are shown in Table 2.2. Damage is introduced for cut-off purposes only. In a recent study [13], the maximum strain for 2024-T3 was given as 18%, so we set the intermediate damage strain ϵ_1 to 0.18. The ultimate damage value is 0.9 at a strain of 0.23.

Table 2.2 Material properties of aluminium 2024 T3

\$	---	5	---	10	---	5	---	20	---	5	---	30	---	5	---	40	---	5	---	50	---	5	---	60	---	5	---	70	---	5	---	80	
\$																																	
PLY	/		1		2					2700.				0							0												
NAME			Ply 1 : Alu																														
			7.240e+10		POWER					0.29				0.0																			
			2.7700e+8		4.8500e+8					0.55																							
					0					0				0.12							0.21						0.18						
										0.0				0.0							0.0						0.0						
																											0.23						

2.3.2 Calibration of Glass Composite Layers

2.3.2.1 Global Ply Model Theory

The global model in Ply TYPE 1 is based on a paper by Ladeveze and Le Dantec [6]. Damage mechanics is used to describe the matrix micro-cracking and fibre/matrix debonding. Internal variables are defined and associated with the progressive loss of rigidity of a ply. It is assumed that the rupture mode in the fibre direction is elastic and brittle and that it does not depend on cyclic loading. Two scalar damage variables are introduced in order to describe the material stiffness reduction under transverse tension and shear loading conditions. The in-plane transverse and shear moduli are modified under the assumption of a progressive damage associated with debonding and micro-cracks parallel to the fibres. The development of these damage variables depends on the static and cyclic loadings and they are coupled. The inelastic strains observed are accounted for via a plastic-hardening model coupled with the damage.

Elastic-Damage Model

Based on the thermodynamic formulae, the density of the free energy can be written, making the plane-stress assumption, in the following form:

$$E_D = \frac{1}{2} \left[\frac{(\sigma_{11})^2}{E_1^0} - \frac{2\nu_{12}^0 \sigma_{11} \sigma_{22}}{E_1^0} + \frac{\langle \sigma_{22} \rangle_+^2}{E_2^0 (1-d')} + \frac{\langle \sigma_{22} \rangle_-^2}{E_2^0} + \frac{(\sigma_{12})^2}{G_{12}^0 (1-d)} \right] \quad (2.2)$$



with

$$\begin{aligned} \langle a \rangle_+ &= a & \text{if } a \geq 0; \text{ otherwise } \langle a \rangle_+ &= 0 \\ \langle a \rangle_- &= a & \text{if } a \leq 0; \text{ otherwise } \langle a \rangle_- &= 0 \end{aligned}$$

where subscripts 1 and 2 denote the fibre and transverse directions, respectively. E_1^0 , E_2^0 , G_{12}^0 , and ν_{12}^0 are the elastic properties of the ply and d and d' are the scalar-damage variables describing the loss of rigidity under shear and transverse tension loading, respectively.

The transverse tension energy and compression energy are split since in compression, micro-cracks close, so no damage is associated with this loading condition. The damage elastic law is thus:

$$\varepsilon_{11}^e = \frac{\sigma_{11}}{E_1^0} - \frac{\nu_{12}^0 \sigma_{22}}{E_1^0} \quad (2.3a)$$

$$\varepsilon_{22}^e = \frac{\langle \sigma_{22} \rangle_+}{E_2^0(1-d')} + \frac{\langle \sigma_{22} \rangle_-}{E_2^0} - \frac{\nu_{12}^0 \sigma_{11}}{E_1^0} \quad (2.3b)$$

$$\varepsilon_{12}^e = \frac{\sigma_{12}}{2G_{12}^0(1-d)} \quad (2.3c)$$

and the thermodynamic forces associated with the damage variables d and d' are obtained:

$$Y_d = \left. \frac{\partial E_D}{\partial d} \right|_{\sigma, d'} = \frac{(\sigma_{12})^2}{2G_{12}^0(1-d)^2} \quad (2.4a)$$

$$Y_{d'} = \left. \frac{\partial E_D}{\partial d'} \right|_{\sigma, d} = \frac{\langle \sigma_{22} \rangle_+^2}{2E_2^0(1-d')^2} \quad (2.4b)$$

The development of the damage depends on these associated forces. Transverse tension/shear coupling is taken into account, based on an equivalent associated force $\underline{Y}(t)$ which is defined from the maximum value observed throughout the loading history (which ensures the damage is “non-healing”):

$$\underline{Y}(t) = \max_{\tau \leq t} \left(\sqrt{Y_d(\tau) + bY_{d'}(\tau)} \right) \quad (2.5a)$$

where b is a transverse tension/shear coupling parameter with default value $= \frac{E_2^0}{G_{12}^0}$ in PAM-CRASH.

Also defined is the transverse damage evolution function:



$$\underline{Y}'(t) = \max_{\tau \leq t} (\sqrt{Y_{d'}(\tau)}) \quad (2.5b)$$

The damage development laws are then very simple and are written as follows:

$$d = \frac{\langle \underline{Y} - Y_0 \rangle_+}{Y_c} \quad \text{if } d < d_{\max}, \underline{Y} < Y_R \text{ and } \underline{Y}' < Y'_s; \text{ otherwise } d = d_{\max} \quad (2.6a)$$

$$d' = \frac{\langle \underline{Y}' - Y'_0 \rangle_+}{Y'_c} \quad \text{if } d' < d_{\max}, \underline{Y} < Y_R \text{ and } \underline{Y}' < Y'_s; \text{ otherwise } d' = d_{\max} \quad (2.6b)$$

The model has damage initiation threshold value Y'_0 in transverse tension, and Y_0 in in-plane shear. Below these initiation values the ply is linear elastic. Above these values the damage parameters (d, d') are linear in the *coupled* energy function $\underline{Y}(t)$ defined in Eq. (2.5a), until one of the brittle damage limits, Y_R (shear damage fracture) or Y'_s (transverse damage limit of the fibre-matrix interface) is reached. The slopes of these linear relationships are determined by Y_c and Y'_c .

Eqs. (2.2-2.6) summarise the main features of the Ladeveze elastic damage model for UD plies. It was assumed in [6] that there is no degradation in the fibre direction so that $d^{ft} = 0$. A further improvement has been added in the PAM-CRASH code. This allows a non-zero fibre damage d^{ft} with a simple form of evolution equation based on tensile fibre direction strains ε^{ft} . The critical parameters are the tensile damage initiation strain ε_i^{ft} and the tensile ultimate failure strain ε_u^{ft} , since the model assumes that damage increases linearly with the strain so that:

$$d^{ft} = d_u^{ft} (\varepsilon^{ft} - \varepsilon_i^{ft}) / (\varepsilon_u^{ft} - \varepsilon_i^{ft}) \quad (2.7)$$

A similar law is implemented in compression. In addition, since it has been observed that fibre misalignment or fibre micro-buckling can lead to non-linear behaviour in the fibre direction under compressive loading, a law for implementing a non-linear modulus in the fibre direction under compressive loading has been implemented:

$$E_1^\gamma = \frac{E_1^{0c}}{1 + \gamma E_1^{0c} |\varepsilon_{11}|} \quad (2.8)$$

where E_1^{0c} is the initial modulus, and the compressive stiffness loss constant, γ , is a material characteristic.

Elastic-Plastic Model

In order to model the inelastic strains induced by damage, an isotropic hardening model was developed and it is coupled with damage via effective quantities based on the equivalent plasticity dissipation Φ_p :

$$\Phi_p = Tr(\sigma \dot{\epsilon}_p) = Tr(\tilde{\sigma} \dot{\tilde{\epsilon}}_p) \quad (2.9)$$

where the effective stresses are defined as:

$$\tilde{\sigma}_{11} = \sigma_{11}, \quad \tilde{\sigma}_{22} = \frac{\langle \sigma_{22} \rangle_+}{1-d} + \langle \sigma_{22} \rangle_-, \quad \tilde{\sigma}_{12} = \frac{\sigma_{12}}{1-d} \quad (2.10)$$

and the effective strains are defined as:

$$\dot{\tilde{\epsilon}}_{11}^p = \dot{\epsilon}_{11}^p, \quad \dot{\tilde{\epsilon}}_{22}^p = \dot{\epsilon}_{22}^p \left(\frac{\langle \sigma_{22} \rangle_+}{\sigma_{22}} (1-d) + \frac{\langle \sigma_{22} \rangle_-}{\sigma_{22}} \right), \quad \dot{\tilde{\epsilon}}_{12}^p = \dot{\epsilon}_{12}^p (1-d) \quad (2.11)$$

In the fibre direction, it is assumed that there is no plastic strain $\dot{\epsilon}_{11}^p = 0$ and that the stress σ_{11} has no effect on the plasticity. The elastic field is defined by the function F :

$$F = \left(\tilde{\sigma}_{12}^2 + A \tilde{\sigma}_{22}^2 \right)^{1/2} - R(p) - R_0 \quad (2.12)$$

where p is the cumulated plasticity index given by $\dot{p} = (4(\dot{\tilde{\epsilon}}_{12}^p)^2 + A(\dot{\tilde{\epsilon}}_{22}^p)^2)^{1/2}$, R_0 is the yield stress and A is the tension-shear plasticity coupling factor, and $R(p)$ is the hardening law such that:

$$R(p) = \beta p^m \quad (2.13)$$

where β and m are coefficients.

2.3.2.2 Glass Composite Calibration Parameters

The parameters for the Global Ply model should be provided from the following experimental test series:

- Tension test on $[0]_8$ laminates
- Tension test with ‘load/unload’ cyclic on $[\pm 45]_{2S}$ laminates
- Tension test with ‘load/unload’ cyclic on $[45]_8$ laminates
- Tension test with ‘load/unload’ cyclic on $[\pm 67.5]_{2S}$ laminates
- Compression test on $[0]_8$ laminates

As mentioned in Section 2.1, none of this data is available for the glass composite layers in Glare. Thus, the parameters had to be estimated somehow. From reference [7], full stress-strain curves in tabulated format for a type of E-glass (Silenka E-glass with MY750 epoxy) were available for transverse and in-plane shear loading. Knowing the moduli for the S2-glass used in Glare (Table 2.1), the E-glass stress values were scaled to match the initial S2-glass moduli.

The resulting two estimated “experimental” stress-strain curves for S2-glass composite for transverse tension and shear loadings, are given in Table 2.3 and 2.4, respectively. Normally the coupling factor b is found from $[\pm 67.5]_{2S}$ laminate tests. However, if this value is just assumed (the default value in PAM-CRASH is E_2^0 / G_{12}^0 or 1.614 here), then the transverse tension and shear damage parameters can be found directly from transverse tension and shear experimental test data. This was the approach used here.

Table 2.3 Estimated “experimental” transverse S2-glass stress-strain curve with resulting calibrated values of d' , \underline{Y}' and \underline{Y}

Strain ε_{22}	Stress σ_{22} (MPa)	d'	\underline{Y}' ($\sqrt{N/m^2}$)	\underline{Y} ($\sqrt{N/m^2}$)
0.00000	0	0.000	0.000	0.000
0.00106	9.97672	0.000	72.716	92.381
0.00230	21.6475	0.000	157.781	200.450
0.00260	24	0.019	178.361	226.595
0.00325	29	0.052	222.951	283.244
0.00380	33	0.077	260.681	331.178
0.00460	38.2	0.118	315.561	400.900
0.00500	40.5	0.139	343.001	435.760
0.00554	43.5	0.166	380.046	482.822
0.00650	48	0.215	445.902	566.488
0.00700	50	0.241	480.202	610.065
0.00800	53.5	0.289	548.8	697.217
0.00900	55.5	0.345	617.4	784.369
0.01000	57	0.394	686	871.521



In the E-glass composite in [7], the transverse modulus is 16.2 GPa and ultimate transverse tensile strength is 40 MPa with an ultimate strain of 0.6%. The transverse modulus of the S2-glass composite in the present research is 9.412 GPa. The “experimental” stress-strain data in Table 2.3 were generated using this modulus with an ultimate transverse strength of 57 MPa and an ultimate strain of 1%. The progressive damage parameter was then calculated as:

$$d' = 1 - \frac{\sigma_{22}}{E_2^0 \varepsilon_{22}}, \text{ and the thermodynamic force } \underline{Y}' \text{ was calculated as: } \underline{Y}' = \frac{\sigma_{22}}{\sqrt{2E_2^0(1-d')}} \text{ (see$$

eqn (2.5b)). The equivalent associated force \underline{Y} was calculated as $\underline{Y} = \sqrt{b}\underline{Y}'$ (see eqn (2.5a)). The initiation threshold was found to be $Y_0' = 200$ in Column 5 of Table 2.3, and the ultimate limit was found to be $Y_s' = 686$ in Column 4. A linear damage evolution between initiation and ultimate state is assumed, and the critical transverse damage limit value (i.e. the inverse of the slope of the line in Fig. 2.1) is obtained as: $Y_c' = 1700$. Fig. 2.1 compares the calibrated linear damage law with the damage values from the “experimental” stress-strain curve.

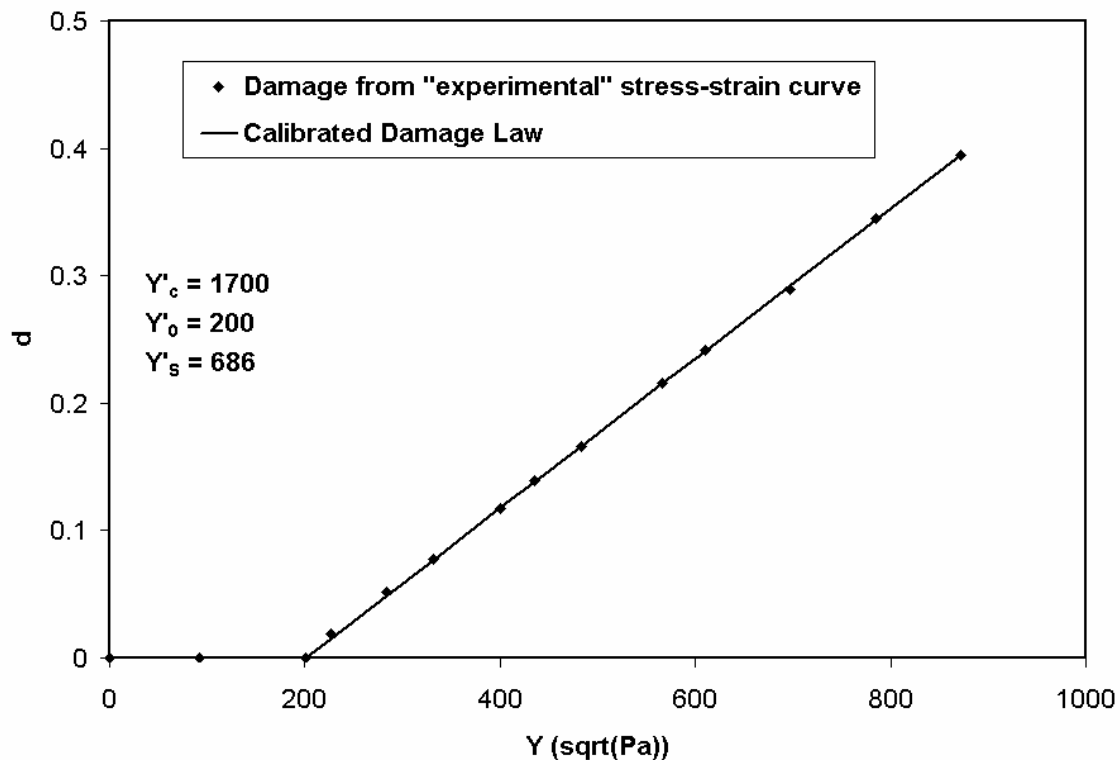


Fig. 2.1 Transverse tension damage law for elementary ply for S2 Glass Composite



Table 2.4 Estimated “experimental” shear S2-glass stress-strain curve with resulting calibrated values of d and \underline{Y}

Strain ε_{12}	Stress σ_{12} (MPa)	d	\underline{Y} ($\sqrt{N/m^2}$)
0.000	0.000	0.000	0.000
0.001	5.830	0.000	53.991
0.002	11.660	0.000	107.981
0.003	17.490	0.000	161.972
0.004	23.320	0.000	215.963
0.005	29.150	0.000	269.954
0.006	34.980	0.000	323.944
0.007	40.180	0.015	372.105
0.008	45.201	0.031	425.159
0.009	50.042	0.046	478.182
0.010	54.703	0.062	531.175
0.011	59.184	0.077	584.134
0.012	63.485	0.093	637.059
0.013	67.606	0.108	689.948
0.014	71.547	0.123	742.799
0.015	75.309	0.139	795.609
0.016	78.891	0.154	848.378
0.017	82.293	0.170	901.102
0.018	85.514	0.185	953.778
0.019	88.557	0.201	1006.405
0.020	91.419	0.216	1058.979
0.021	94.101	0.231	1111.498
0.022	96.604	0.247	1163.957
0.023	98.926	0.262	1216.354
0.024	101.069	0.278	1268.684
0.025	103.032	0.293	1320.943
0.026	104.815	0.309	1373.127
0.027	106.418	0.324	1425.230
0.028	107.841	0.339	1477.247
0.029	109.085	0.355	1529.171
0.030	110.148	0.370	1580.997
0.032	113.336	0.392	1666.594
0.034	114.904	0.420	1751.607
0.035	115.177	0.436	1840.049
0.037	116.557	0.460	1912.315
0.038	116.281	0.475	1992.938
0.039	116.226	0.489	2050.673
0.040	116.191	0.502	2105.003



Data in Table 2.4 were created using shear modulus 5.83GPa, which is taken directly from the value for E-glass/MY750 in [7]. The shear progressive damage parameter is thus computed using $d = 1 - \frac{\sigma_{12}}{G_{12}^0 \gamma_{12}}$. Only an elastic damage model (no plastic deformation) is considered in this calibration due to lack of material properties. The thermodynamic force \underline{Y} is calculated as: $\underline{Y} = \frac{\sigma_{12}}{\sqrt{2G_{12}^0(1-d)}}$ (see eqn 2.5(a)). In this case, the initiation is found at $Y_0 = 324$, and ultimate state at $Y_R = 2105$. As in transverse tension, a linear damage evolution between initiation and ultimate state is assumed, and the critical shear damage limit value (i.e. the inverse of the slope of the line in Fig. 2.2) is obtained as: $Y_c = 3500$.

These obtained damage parameters from transverse tension and shear loadings form the data in CARD 5 of PLY 1 in PAM-CRASH. The coupling factor between shear and transverse damage was set to the default value $b = \frac{E_2^0}{G_{12}^0}$, and the maximum allowed damage value for shear damage and transverse damage was taken as $d_m = 0.95$ as recommended in [8]. All ply data for UD glass are given in Table 2.6. A single element test using this ply data was performed to obtain both transverse tension and shear stress-strain curves, which are presented in Figs 2.3 and 2.4, respectively. It can be seen that the predicted results gave good agreement with the “experimental” data.

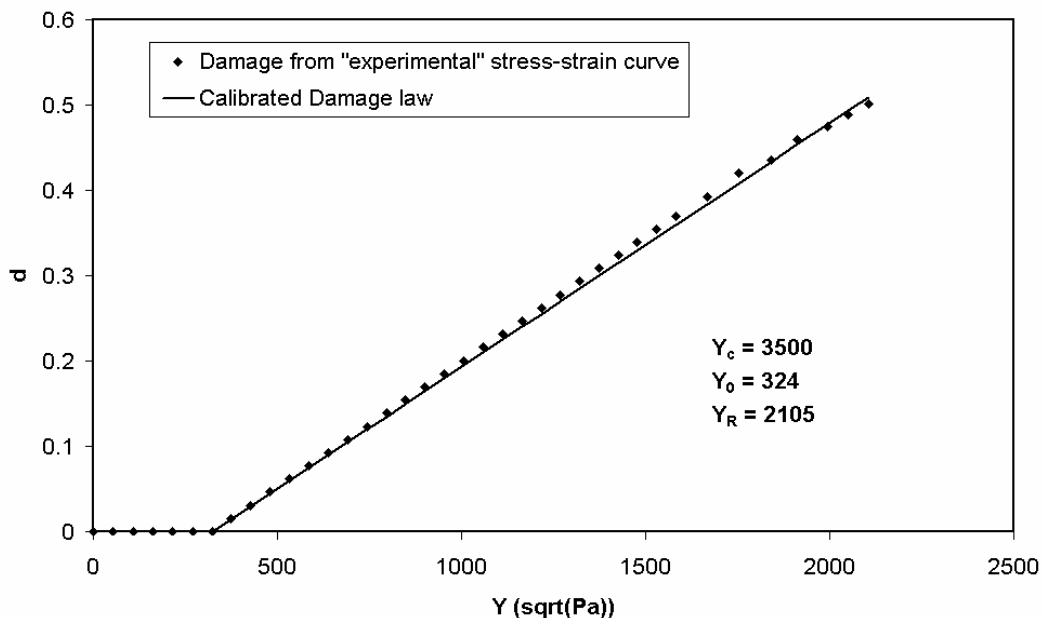


Fig. 2.2 Shear damage law for elementary ply for S2 Glass Composite



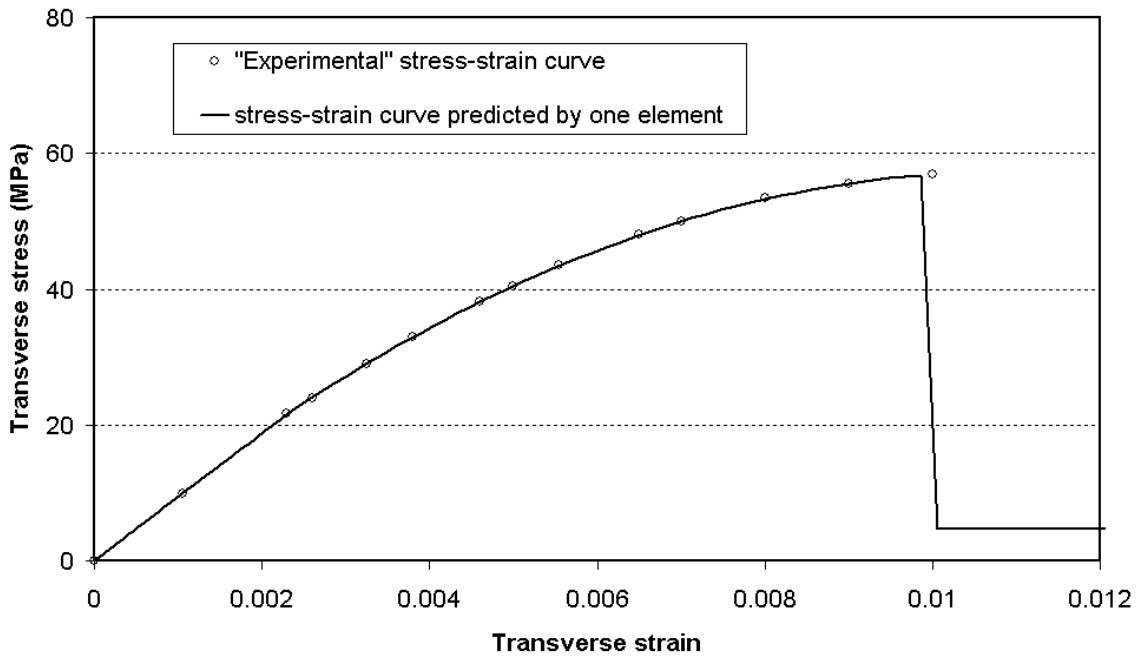


Fig. 2.3 Transverse tension behaviour of elementary ply for S2 Glass Composite

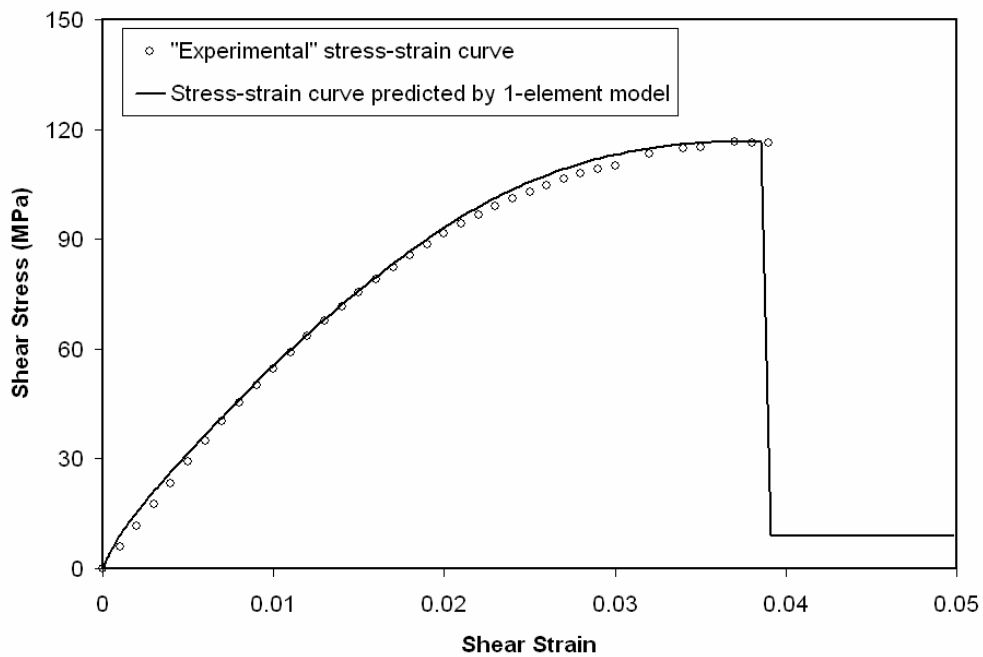


Fig. 2.4 Shear behaviour of elementary ply for S2 Glass Composite

As mentioned in the Theory section above, ESI has added the capability for non-zero fibre damage in the Global Ply model. The parameters needed for this in tension are ε_i^{ft} , ε_u^{ft} and d_u^{ft} . Carbon-fibre reinforced composites tested in the fibre direction show a brittle linear elastic behaviour in tension and a brittle non-linear elastic behaviour in compression [7]. We assume here that glass-fibre reinforced composites have similar behaviour in the fibre direction.

From reference [9], the tensile axial elongation at failure of S-glass fibre is 5.7%. Thus the values $\varepsilon_i^{ft} = 0.056$, $\varepsilon_u^{ft} = 0.067$ and $d_u^{ft} = 0.99$ were used. With these values (see CARD 6 of the ply data in Table 2.6), the tensile behaviour of the S-glass composite was obtained from a single element test as shown in Fig. 2.5.

The compressive non-linear stress-strain relationship is for now simply guessed and is given in Table 2.5. From this the continuously varying compressive secant modulus is calculated (Column 3). The slope of the best fit line through a plot of modulus versus stress (Fig. 2.6) then gives the parameter γ in equation (2.8) to be $\gamma = 4.187 \times 10^{-10}$. A single-element test in PAM-CRASH using this γ value confirms that the model matches the “experimental” data (Fig. 2.7).

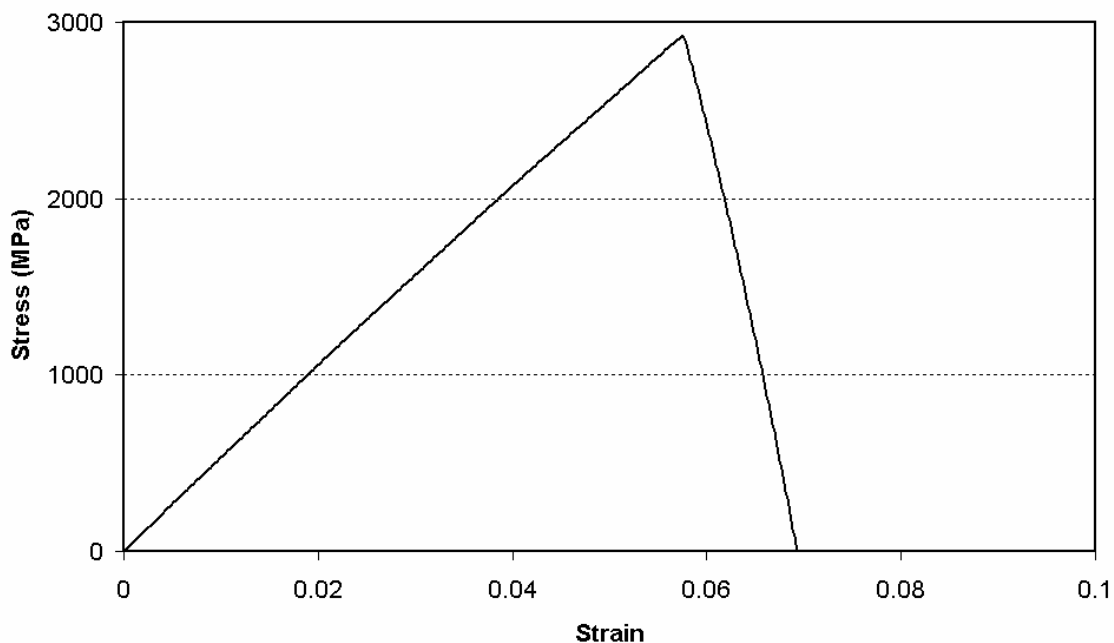


Fig. 2.5 Tensile behaviour (in fibre direction) of elementary ply for S2 Glass Composite

Table 2.5 Estimated variation of compressive Young's modulus for S2 glass

Strain	Stress (MPa)	E_1^c (GPa)
0	0	53.98
0.001	53	53
0.002	104	52
0.003	153	51
0.004	200	50
0.005	245	49
0.006	288	48
0.007	329	47
0.009	405	45
0.012	510	42.5
0.015	607.5	40.5
0.017	663	39
0.019	722	38
0.021	777	37
0.023	828	36
0.025	875	35
0.027	918	34
0.029	957	33
0.031	992	32
0.033	1023	31
0.035	1057	30.2
0.037	1091.5	29.5
0.039	1119.3	28.7
0.041	1152.1	28.1
0.043	1182.5	27.5
0.045	1215	27



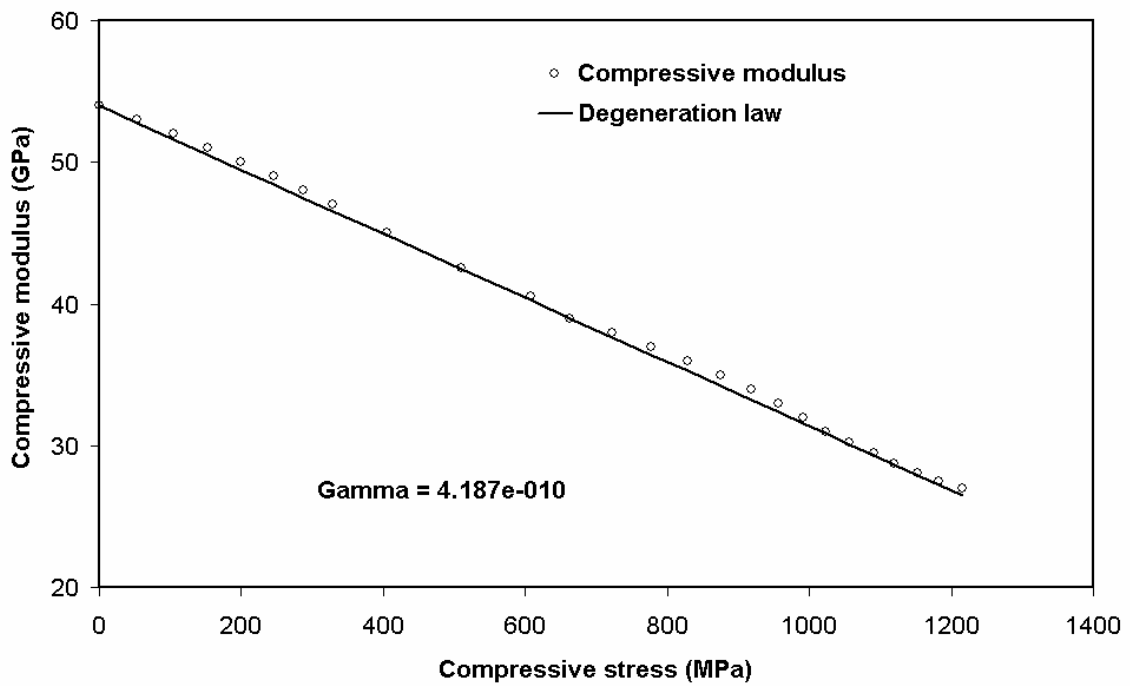


Fig. 2.6 Compressive modulus degeneration of elementary ply for S2 Glass Composite

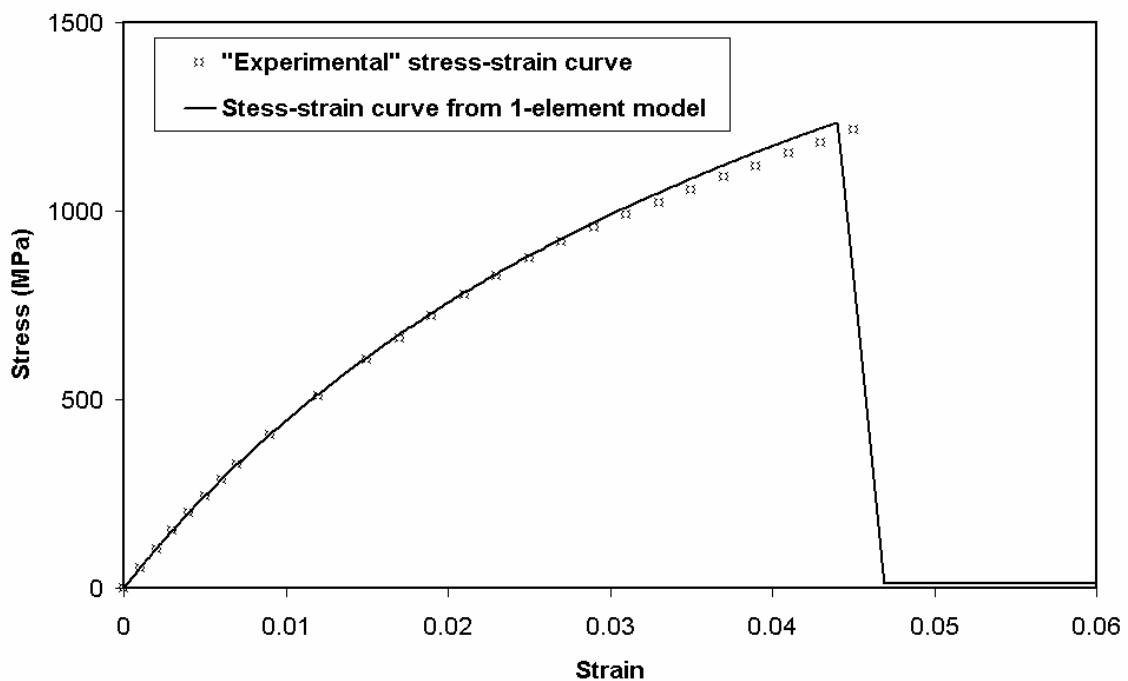


Fig. 2.7 Compressive behaviour of elementary ply for S2 Glass Composite

Finally, the full, calibrated PLY data for the glass layers are given in Table 2.6.

Table 2.6 Calibrated PLY data for UD S2 glass composite

\$ Glass Fibre Composite Properties (preliminary calibration)									
\$									
PLY	/	3	1	1550.	0	0			
NAME glass fiber									
53.98e+009		9.41e+009							
5.83e+009		5.83e+009		0.28	0.0	0.0			
	3500.01	323.944	1700.00	200.00	1.61	686.00	2105.45	0.25	
	0.056	0.067	0.99						
53.98e+009	4.187e-010		0.045	0.048	0.99				

2.3.3 Glare quasi-static 45° test models

Having determined preliminary calibrations for the aluminium alloy and glass composite layers, these calibrations were incorporated into a Glare model with the same lay-up as that in the UOXF tests [1]. This section examines the resulting simulations of UOXF's 45° quasi-static tensile tests.

For simplicity, two 4×4 mm elements were used to model the 8×4 mm gauge section of the UOXF specimen. A detailed model of the UOXF specimen (including the curved specimen geometry) provided by ESI, proved too time-consuming for these preliminary calibrations, particularly when calibrating rate effects. The more detailed model may be used in post-test calibrations.

The Ply TYPE 2 data in Table 2.2 and TYPE 1 data in Table 2.6 were used directly in forming the lay-up (A/0/90/A/90/0/A) of the Glare specimen. Predicted results from testing in the 45° direction are shown in Fig. 2.8 (red line). It can be seen that a sudden load drop occurs at an extension of 0.0002m, which reflects the shear failure of the glass plies (at 4% shear strain in the plies – see Fig. 2.4 for the calibrated shear properties). Clearly this did not happen in the test, and the glass layers seem to have survived to higher shear strains than expected. In fact, the high shear failure strains exhibited are reminiscent of the behaviour in ±45° tests of fabric materials. It is known [10] that provided layers do not delaminate, they interact in their failure behaviour, so it may be that the + and - 45° layers in this test behaved in a similar fashion to a single ±45° fabric layer up to high strain levels, thus explaining the high failure strains.

Due to a lack of material properties for UD S-glass plies, we modified the model to consider this interaction effect, by simply decreasing the damage cut-off value d_{max} from 0.95 to 0.25. The modified results are also shown in Fig. 2.8 (blue line). The value of 0.25 was chosen to provide a match of the ultimate strength of Glare in the 45° tests. It is noticeable that both predicted ultimate failure extensions are substantially higher than the experimental result. This

is due to the cut-off strain used for the aluminium alloy. Unfortunately, this value, shown in Table 2.2, cannot be lowered as it was determined by matching test results in 0^0 direction.

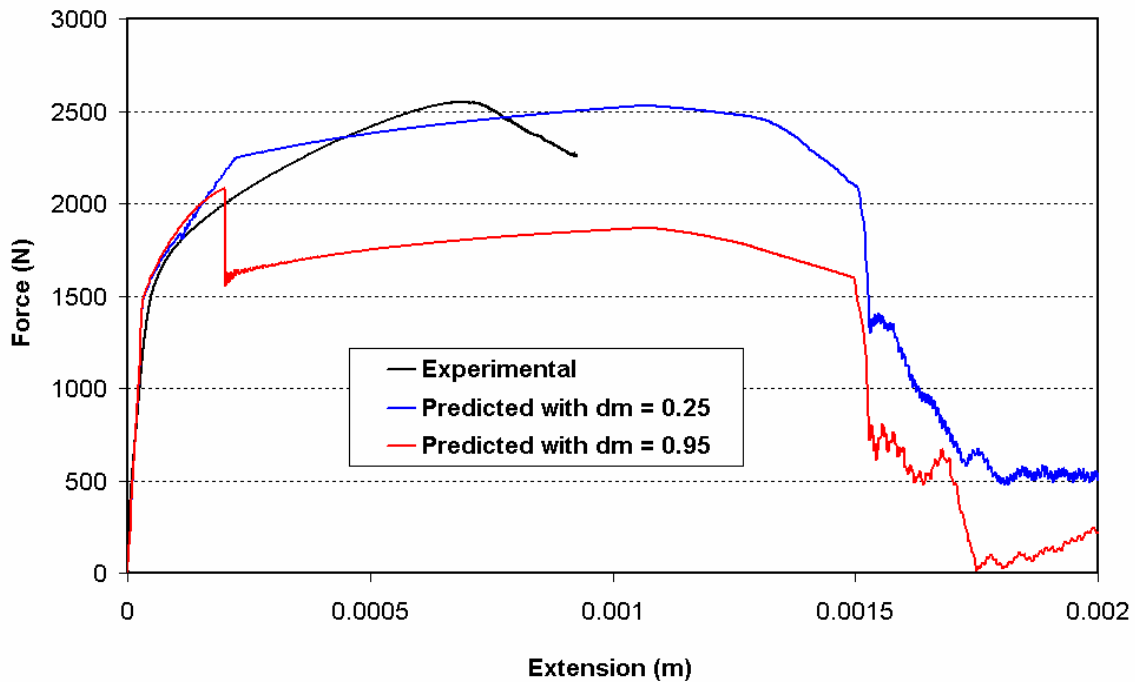


Fig. 2.8 Predicted force-extension relationship and experimental results of Glare under quasi-static tension in the 45^0 direction

2.3.4 Glare quasi-static 0^0 test models

From D.1.1.8 [1], it can be seen that Glare exhibited similar properties under tension in 0^0 and 90^0 directions. Thus, only the 0^0 direction tests are modelled here.

The predicted tensile response is presented in Fig. 2.9. Excellent agreement is obtained between the predicted results and test data except the ultimate strength is slightly over-estimated. From a modelling point of view, this over-estimation could be removed by introducing an intermediate value for the fibre damage in PAM-CRASH (presently only initial and ultimate values are allowed, making for a completely linear behaviour up to failure). Whether such a change is valid physically however, is open to debate. It will be shown in the next section that this would also help in matching the behaviour at high strain rate loading conditions.

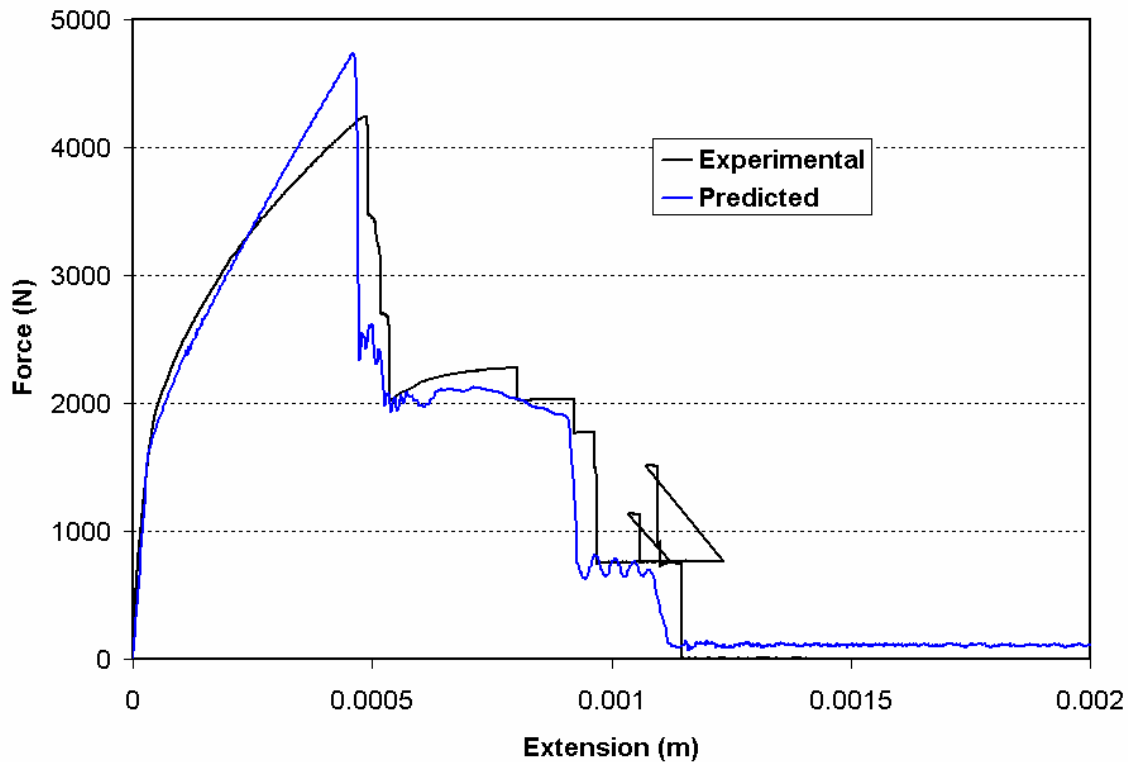


Fig. 2.9 Predicted force-extension relationship and experimental results of Glare under quasi-static tension in the 0^0 direction

2.4 Material Calibration II: High strain rate effects

As described in [8] strain rate effects are observed in steel and aluminium alloys in their plastic behaviour where the strain hardening functions may be significantly rate dependant. Global models have been developed in which the plastic hardening curve is multiplied by a dynamic increase factor (DIF) which contains a number of parameters, e.g. as in the Johnson-Cook and Cowper-Symonds rate dependent laws.

Unidirectional composite materials containing organic resins can display strain rate sensitivity during loadings. Matrix dominated modes are thus likely to be strain rate dependent in all fibrous composites. In the case of glass and aramid composites the fibres also show some viscoelasticity, so strain rate effects are seen during loading in the fibre direction. Indeed, as stated in Section 2.2, reference [5] cites several studies that have shown that the strain rate sensitivity of glass/epoxy in the fibre direction is very significant.

Experimental studies on UD composites for various load velocities have displayed the two following main observations [11]:

- There is always a threshold from which the strain rate strongly influences the laminate behaviour: a reference curve can thus be identified.

- There are also significant increases in elastic moduli, rupture stresses and yield stress that can be described by suitable laws of evolution.

These observations allowed the development of an original approach based on the concept of viscous stress.

2.4.1 PAM-CRASH strain rate modelling theory

The modelling involves splitting up the stress into an elastic stress (σ^e) and a stress corresponding to the viscous phenomena (σ^v):

$$\sigma = \sigma^e + \sigma^v \quad (2.14)$$

This allows the definition of some functions of viscosity (F_{ij}) that can be applied to each elastic modulus. The constitutive relationships then become:

$$\begin{Bmatrix} \sigma_{11} \\ \sigma_{22} \\ \sigma_{12} \\ \sigma_{13} \\ \sigma_{23} \end{Bmatrix} = \begin{pmatrix} C_{11} & \nu_{12}^0 C_{11} & 0 & 0 & 0 \\ \nu_{21}^0 C_{11} & C_{22}(1-d_{22}) & 0 & 0 & 0 \\ 0 & 0 & C_{12}(1-d_{12}) & 0 & 0 \\ 0 & 0 & 0 & G_{13}^0 & 0 \\ 0 & 0 & 0 & 0 & G_{23}^0 \end{pmatrix} \begin{Bmatrix} \varepsilon_{11}^e \\ \varepsilon_{22}^e \\ 2\varepsilon_{12}^e \\ 2\varepsilon_{13}^e \\ 2\varepsilon_{23}^e \end{Bmatrix} \quad (2.15)$$

where $C_{ij} = C_{ij}^0(1 + F_{ij}(\dot{\varepsilon}))|_{i,j=1,2}$ and $C_{ij}^0 = E_{ii}^0|_{i=j}$ else $C_{ij}^0 = G_{ij}^0|_{i \neq j}$

These three viscosity functions applied thus to the elastic moduli, define implicitly the damage functions:

$$d = \frac{\langle Y(t) - \underline{Y}_0 \rangle_+}{\underline{Y}_c} \quad \text{if } d < d_m, \quad Y(t) < Y_R \quad \text{and } Y' < Y'_s; \quad \text{otherwise } d = d_m \quad (2.16a)$$

$$d' = \frac{\langle Y(t) - Y'_0 \rangle_+}{\underline{Y}'_c} \quad \text{if } d' < d_m, \quad Y(t) < Y_R \quad \text{and } Y' < Y'_s; \quad \text{otherwise } d' = d_m \quad (2.16b)$$

where

$$\underline{Y}_c = (Y_c) \sqrt{(1 + F_{12}(\dot{\varepsilon}))} \quad (2.17a)$$

$$\underline{Y}_0 = (Y_0) \sqrt{(1 + F_{12}(\dot{\varepsilon}))} \quad (2.17b)$$

$$\underline{Y}'_c = (Y'_c) \sqrt{(1 + F_{12}(\dot{\varepsilon}))} \quad (2.17c)$$

$$\underline{Y}'_0 = (Y'_0) \sqrt{(1 + F_{12}(\dot{\varepsilon}))} \quad (2.17d)$$

The fibre direction rupture stresses evolution is taken into account, in tension and compression, using the longitudinal strain evolutions:

$$\underline{\varepsilon}_{i,u}^{ft} = \varepsilon_{i,u}^{ft} (1 + F_{11}^R(\dot{\varepsilon})) \text{ in tension} \quad (2.18a)$$

$$\underline{\varepsilon}_{i,u}^{fc} = \varepsilon_{i,u}^{fc} (1 + F_{11}^R(\dot{\varepsilon})) \text{ in compression} \quad (2.18b)$$

Finally, the evolution of plastic flow is given by the evolution of yield stress:

$$f(\underline{\sigma}, R) = \sqrt{\left[\frac{\sigma_{12}}{(1-d)} \right]^2 + A \left[\frac{\langle \sigma_{22} \rangle_+}{(1-d')} + \langle \sigma_{22} \rangle_- \right]^2} - (R_0 + \beta(\varepsilon^p)^m) \quad (2.19)$$

where $R_0 = R_0(1 + F_R(\dot{\varepsilon}))$.

In summary, the strain rate sensitivity of UD composite behaviour uses five functions of evolution:

$F_{11}(\dot{\varepsilon})$ for longitudinal Young's modulus

$F_{22}(\dot{\varepsilon})$ for transverse Young's modulus

$F_{12}(\dot{\varepsilon})$ for shear modulus

$F_{11}^R(\dot{\varepsilon})$ for longitudinal rupture strain

$F_R(\dot{\varepsilon})$ for yield stress

Three rate-dependent laws can be used:

Power law:
$$F_{ij}(\dot{\varepsilon}) = 1 + D_{ij} \left(\frac{\dot{\varepsilon}}{\dot{\varepsilon}_{ij}^{ref}} \right)^{n_{ij}} \quad (2.20a)$$

Linear law:
$$F_{ij}(\dot{\varepsilon}) = 1 + D_{ij} \left(\frac{\dot{\varepsilon}}{\dot{\varepsilon}_{ij}^{ref}} \right) + n_{ij} \quad (2.20b)$$

Neperian logarithmic law:
$$F_{ij}(\dot{\varepsilon}) = 1 + D_{ij} \log \left(\frac{\dot{\varepsilon}}{\dot{\varepsilon}_{ij}^{ref}} \right) + \log(n_{ij}) \quad (2.20c)$$

where D_{ij} and n_{ij} are parameters to be measured and $\dot{\varepsilon}_{ij}^{ref}$ is a reference strain rate. These laws can be used independently.

2.4.2 High Strain Rate Calibration Parameters

High strain rate tests have been performed by UOXF at two distinct strain rates:

- Medium rate (MR) $\dot{\epsilon} = 100s^{-1}$
- High rate (HR) $\dot{\epsilon} = 3300s^{-1}$

Two types of experimental results i.e. elastic properties and strength properties were reported in D1.1.8 [1]. From the results of the uniaxial tensile tests for elastic properties, very little rate dependency was evident for elastic moduli E_{11} , E_{22} and G_{12} , or poisson ratios ν_{12} and ν_{21} as shown in Table 2.7.

Table 2.7 Elastic properties of Glare under high strain rates (from [1])

	QS	MR	HR
E_{11}	60.1	61.4	62.2
E_{22}	59.1	59.5	58.9
G_{12}	26.6	26.7	26.8
ν_{12}	0.298	0.305	0.306
ν_{21}	0.30	0.305	0.315

However, the results for *strength* properties of Glare under high strain rates indicated considerable increase in ductility, as shown in Figs. 2.10 and 2.11 for the 0° and 45° direction, respectively. For a rate increase from quasi-static to $3300s^{-1}$, the ultimate load capacity (tensile strength) of Glare in the 0° direction increased from 4200 N to 5000 N, while the ultimate extension (strain) approximately doubled (Fig. 2.9). No increase is found for tensile strength in the 0° direction under medium rate loading ($\dot{\epsilon} = 100s^{-1}$). As mentioned at the beginning of this section, there is always a threshold from which the strain rate strongly influences the laminate behaviour. We may conclude that the strain rate of $\dot{\epsilon} = 100s^{-1}$ is below this threshold in this material. Another reason why strain rate effects are not seen at the medium loading rate may be because the test strain rate is not really $100s^{-1}$. From the strain rate-time relationship in Fig. 63 (page 46) of D.1.1.8 [1], it can be seen that the $100s^{-1}$ strain rate only existed for a very short period of the test, and in fact, viewing the force in Fig. 64, it can be seen that the specimens failed (after about 4 ms) before the strain rate rose above $50s^{-1}$. In fact the average strain rate up to specimen failure was about $20 - 30s^{-1}$.

In the 45° tests (Fig. 2.11), substantial increase is seen in maximum extension, with minor increase in capacity (strength). Examining Figs. 71 and 72 in [1] shows that the average strain rate in the medium rate tests up to specimen failure was about $75s^{-1}$, considerably higher than in the 0° case, but still less than $100s^{-1}$. We postulate here that the increase in maximum extension at high strain rates (compared to quasi-static rates) is due to the strain rate sensitivity of the “interaction” effect discussed in Section 2.3.3 between the $+45^\circ$ and the -45° glass layers. At low strain rates, shear cracks and delamination have time to develop,



eventually separating these layers so they can fail independently. At higher strain rates, delaminations do not have time to develop, so that the $+45^\circ$ and the -45° layers behave like a single $\pm 45^\circ$ fabric layer for longer, resulting in higher failure strains. Apparently, this effect, if it exists, is activated at strain rates below that of the medium rate tests, since the maximum extension is similar in the medium and high rate tests.

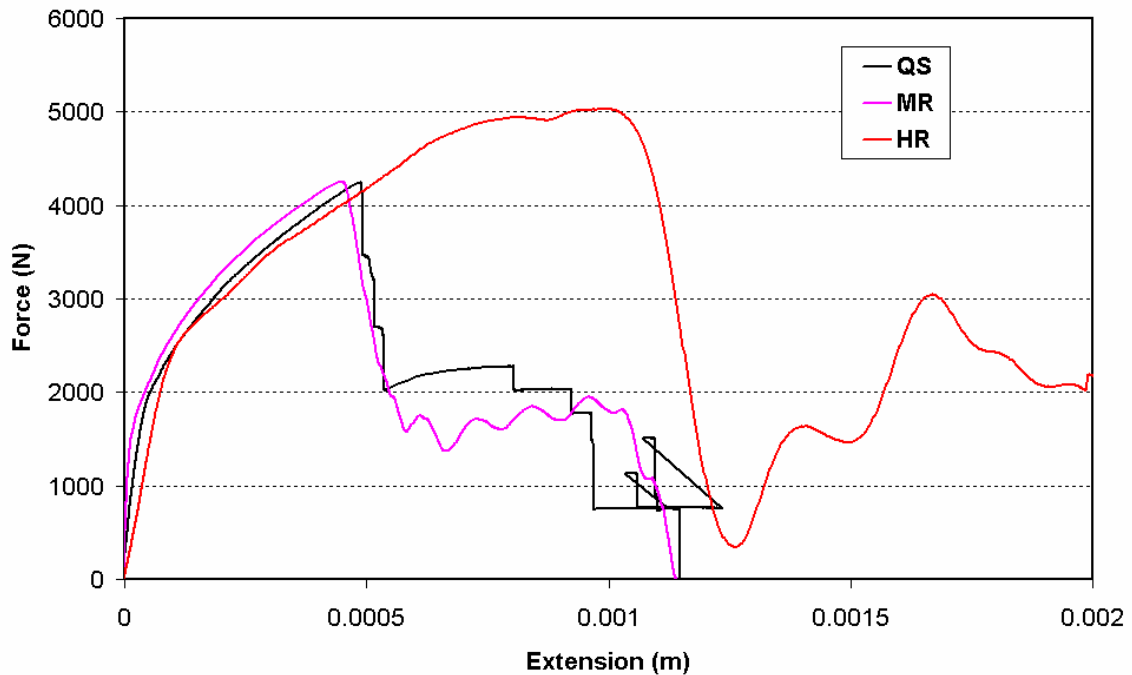


Fig. 2.10 Experimental force-extension curves of Glare under different strain rates when loaded in the 0° direction (from [1])

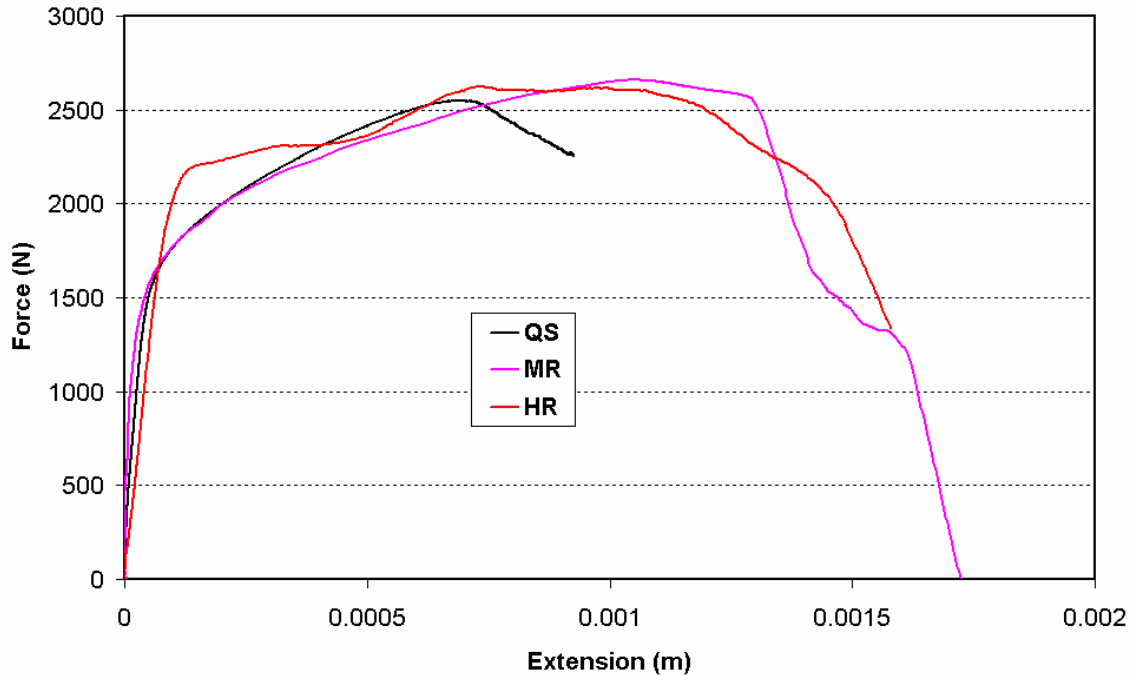


Fig. 2.11 Experimental force-extension curves of Glare under different strain rates when loaded in the 45° direction (from [1])

To try to match these observations, it is assumed here that the longitudinal Young's modulus of the glass composite layers is strain-rate independent (i.e. $F_{11}(\dot{\epsilon}) = 1$), but transverse modulus, shear modulus and longitudinal rupture strain are rate dependent. The yield stress of glass composite should be rate dependent, but as discussed in section 2.3.2, the effects of plastic deformation were not considered in the damage model, so $F_R(\dot{\epsilon})$ was set to 1.

The three proposed rate dependent laws for fibre ultimate strain $\epsilon_{i,u}^{ft}$, transverse modulus E_{22} , and shear modulus G_{12} are shown in Figs. 2.12, 2.13 and 2.14 respectively. A value of $100s^{-1}$ was used for the reference strain rate $\dot{\epsilon}_{ij}^{ref}$ in all three laws. The strain rate parameters proposed for each property are shown in each figure. Parameters in Fig. 2.12 form a DIF = 2.02 for fibre ultimate strain $\epsilon_{i,u}^{ft}$ at strain rate $\dot{\epsilon} = 3300s^{-1}$, which is designed to meet the test results. This is the only value we can extract from the tests for defining the rate dependent laws. Although there is no increase found from the 0° test results at a strain rate $\dot{\epsilon} = 100s^{-1}$, we still propose a DIF = 1.49 for the fibre ultimate strain at this rate because the true test rate was less than $100s^{-1}$.

Proposed parameters in Figs. 2.13 and 2.14 generate a DIF = 1.36 at $\dot{\epsilon} = 3300s^{-1}$ and DIF = 1.22 at $\dot{\epsilon} = 100s^{-1}$ for transverse modulus, and a DIF = 1.47 at $\dot{\epsilon} = 3300s^{-1}$ and DIF = 1.32 at $\dot{\epsilon} = 100s^{-1}$ for shear modulus.

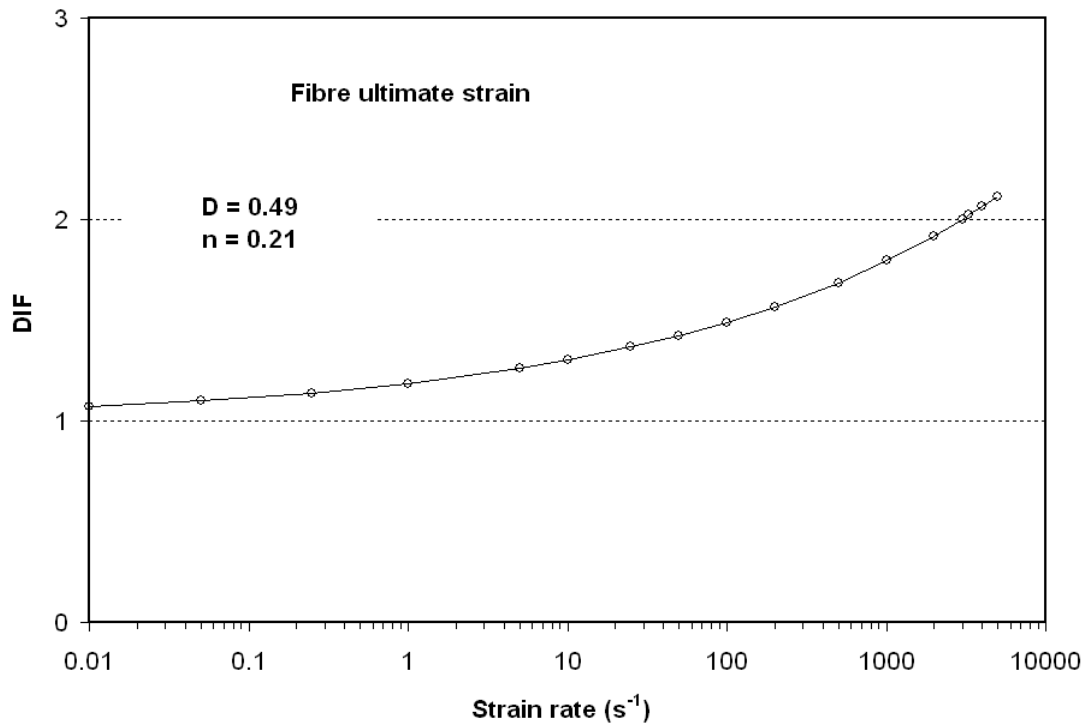


Fig. 2.12 Proposed strain rate law for fibre ultimate strain $\epsilon_{i,u}^{ft}$

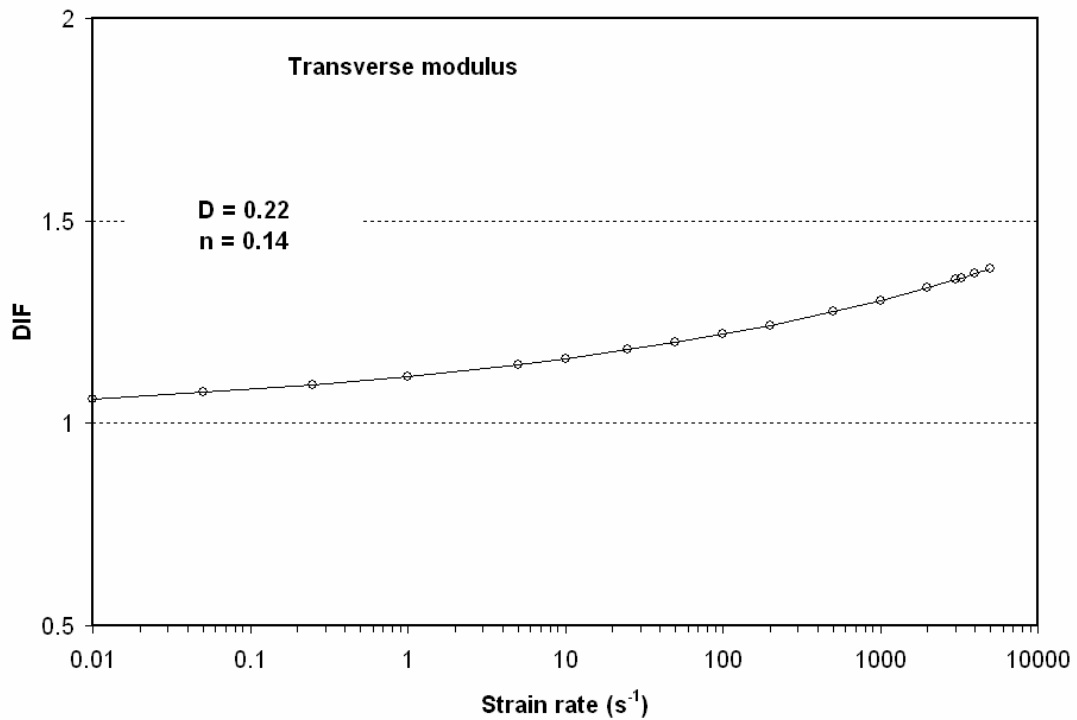


Fig. 2.13 Proposed strain rate law for transverse modulus E_{22}



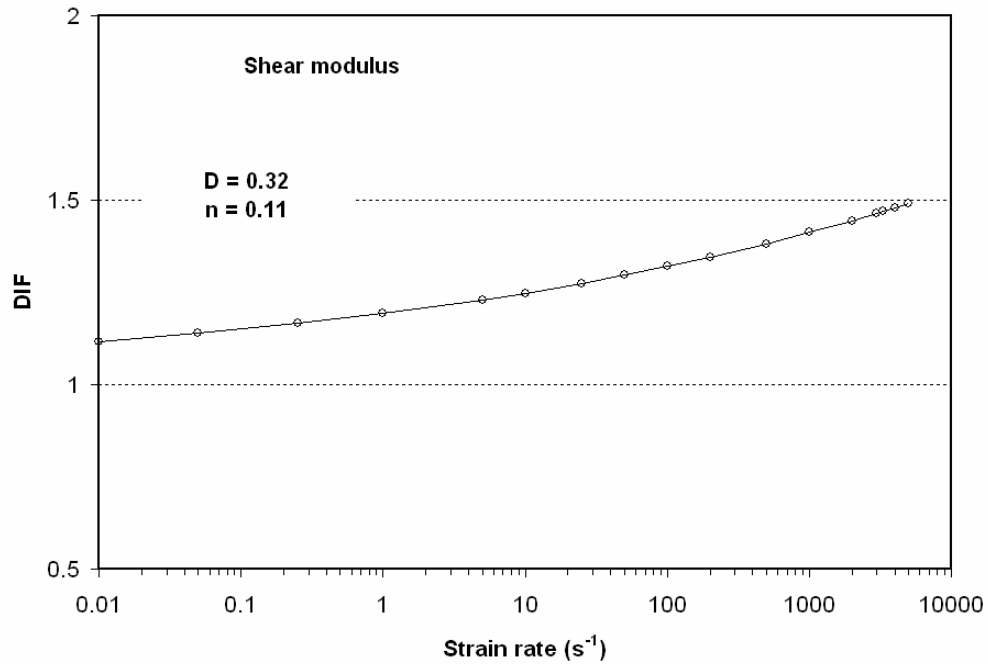


Fig. 2.14 Proposed strain rate law for shear modulus G_{12}

Medium and high strain rate simulations were then carried out using the two-element model of the gauge section of the UOXF specimen, as described in Section 2.3.3. In these simulations, the recorded velocity time history for each test was digitised from [1] and used to apply the displacement (see Figs. 2.15-2.18).

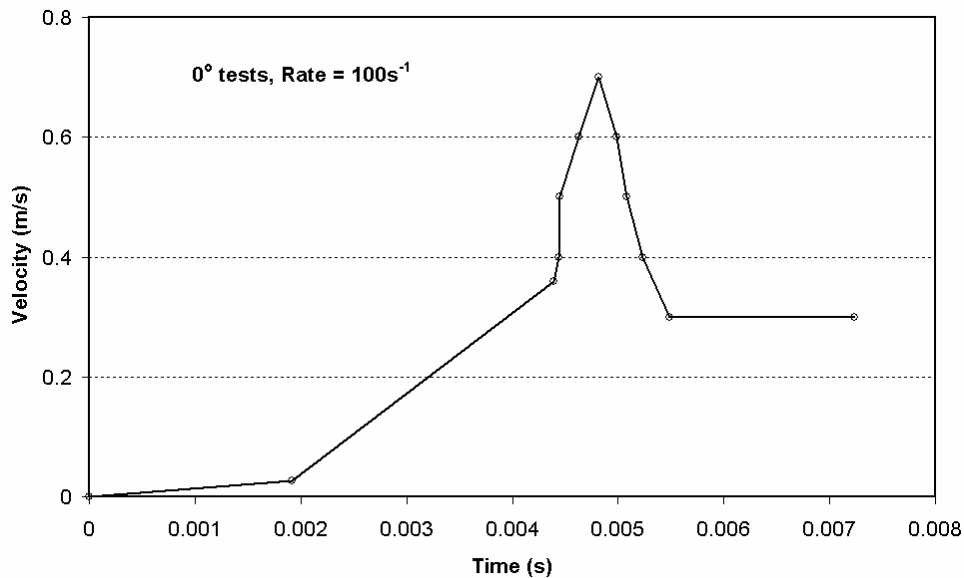


Fig. 2.15 Velocity time history used in simulations of medium rate test in 0-direction



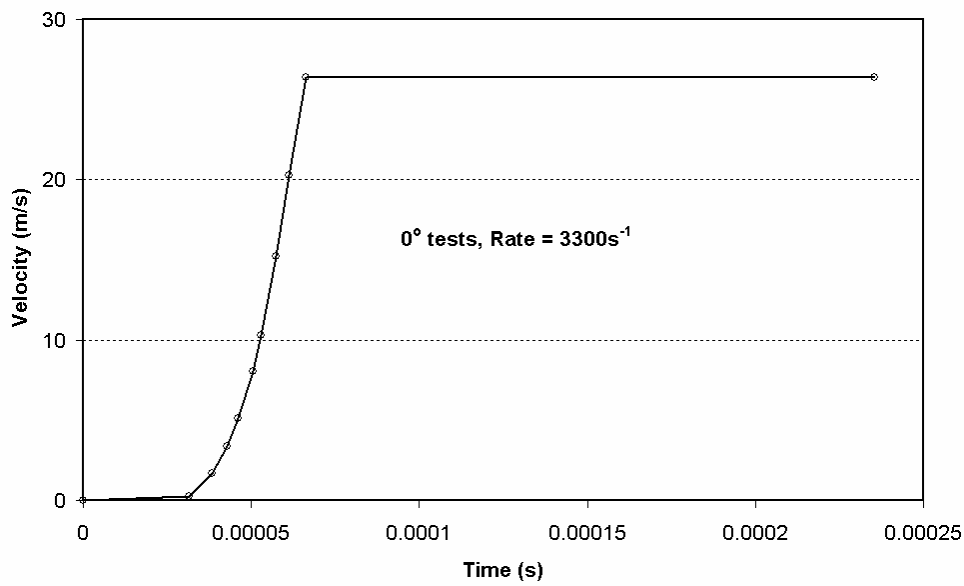


Fig. 2.16 Velocity time history used in simulations of high rate test in 0-direction

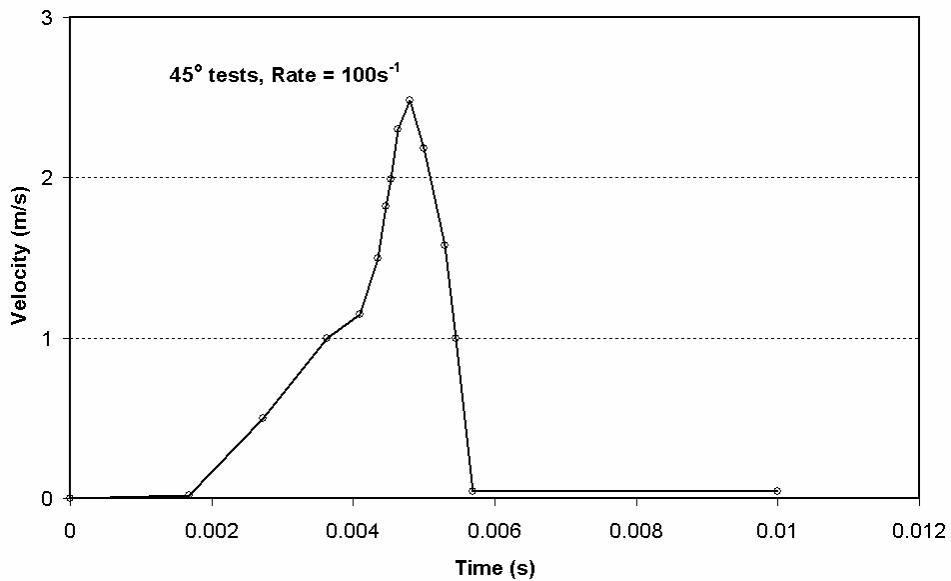


Fig. 2.17 Velocity time history used in simulations of medium rate test in 45-direction

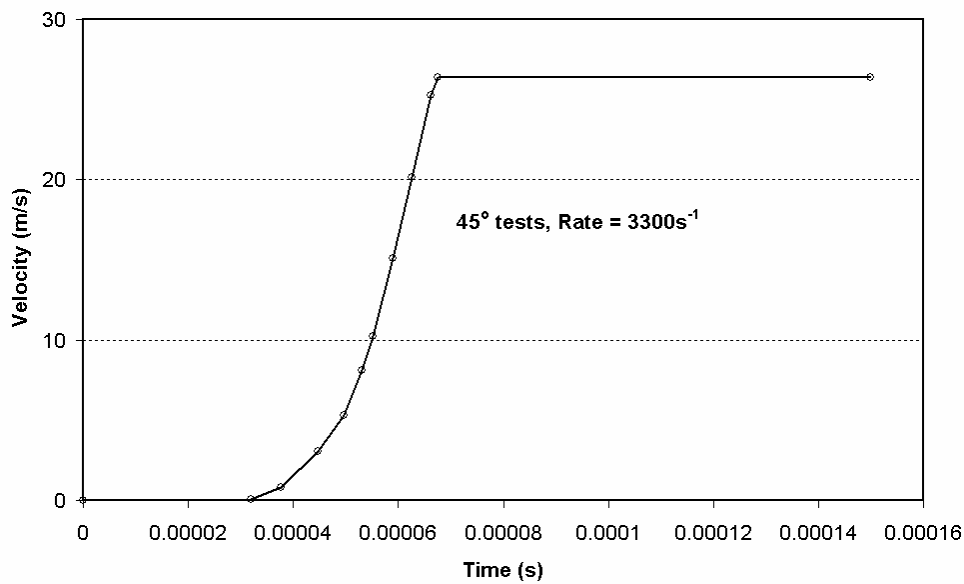


Fig. 2.18 Velocity time history used in simulations of high rate test in 45-direction

The simulated results are presented with the experimental results in Figs. 2-19-2.22. From these figures, the simulations show very good agreement with experiment for the medium strain rate ($\dot{\epsilon} = 100s^{-1}$) in both 0° and 45° directions. However, the present model gives over-estimated results with strain rate $\dot{\epsilon} = 3300s^{-1}$ in both 0- and 45-directions. The results in 0° direction could again be improved by the introduction of an intermediate damage value for damage in the fibre direction. The over-estimated results in 45° direction implies that the strain rate parameters used (particularly for shear modulus) may be too high. However, given the quite variable results seen in the literature for high strain rate testing of composites, the calibrations shown here are considered quite acceptable for a preliminary calibration.

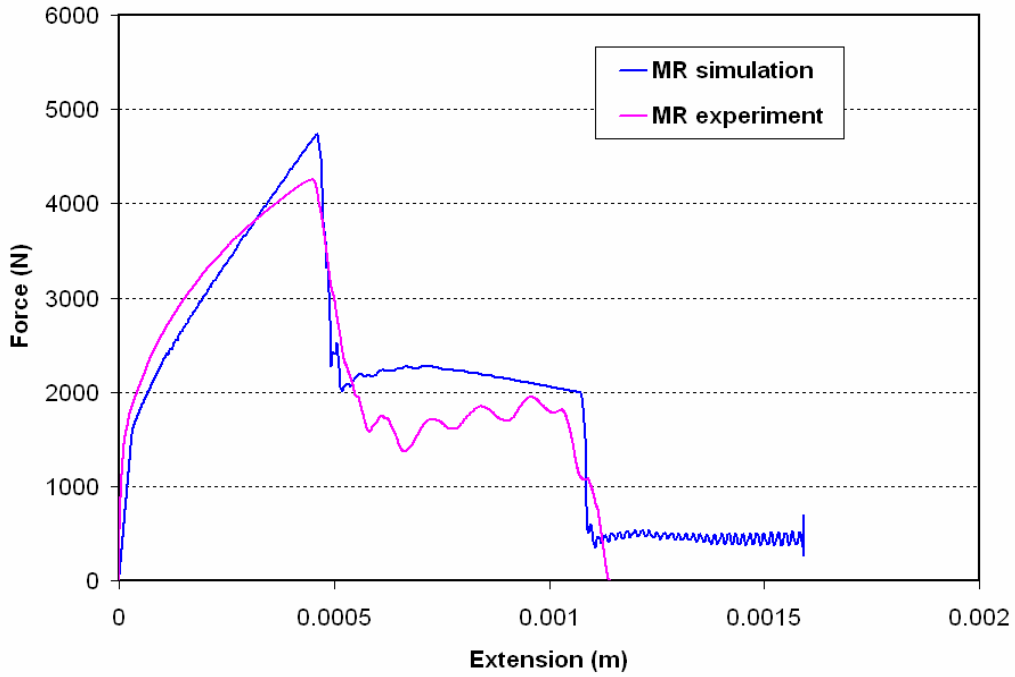


Fig. 2.19 Predicted force extension relationship and the experimental results with rate $\dot{\epsilon} = 100s^{-1}$ in 0-direction

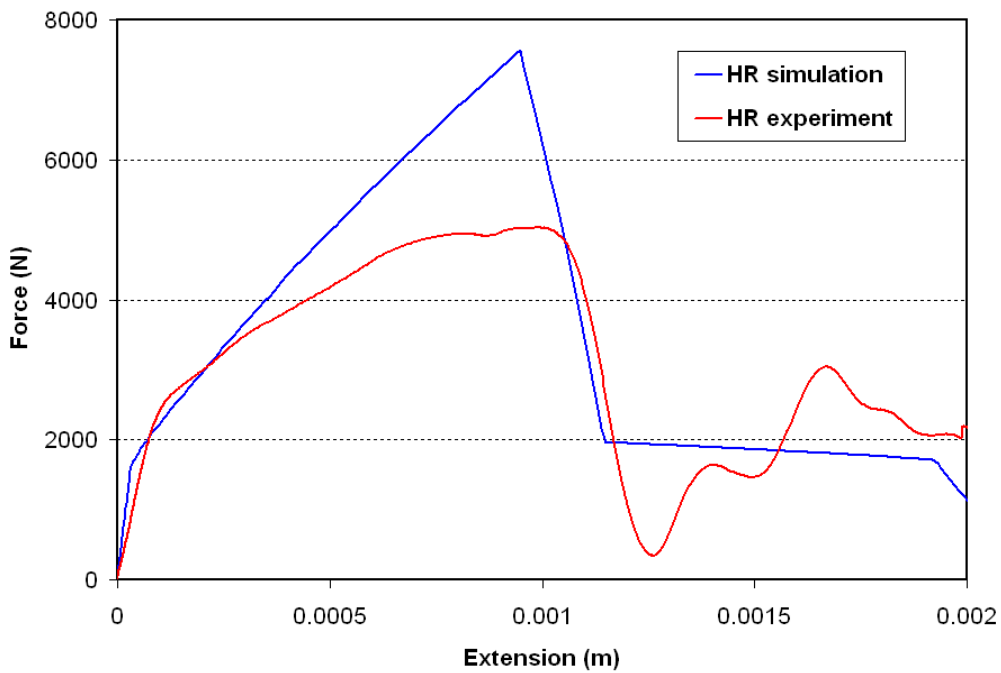


Fig. 2.20 Predicted force extension relationship and the experimental results with rate $\dot{\epsilon} = 3300s^{-1}$ in 0-direction



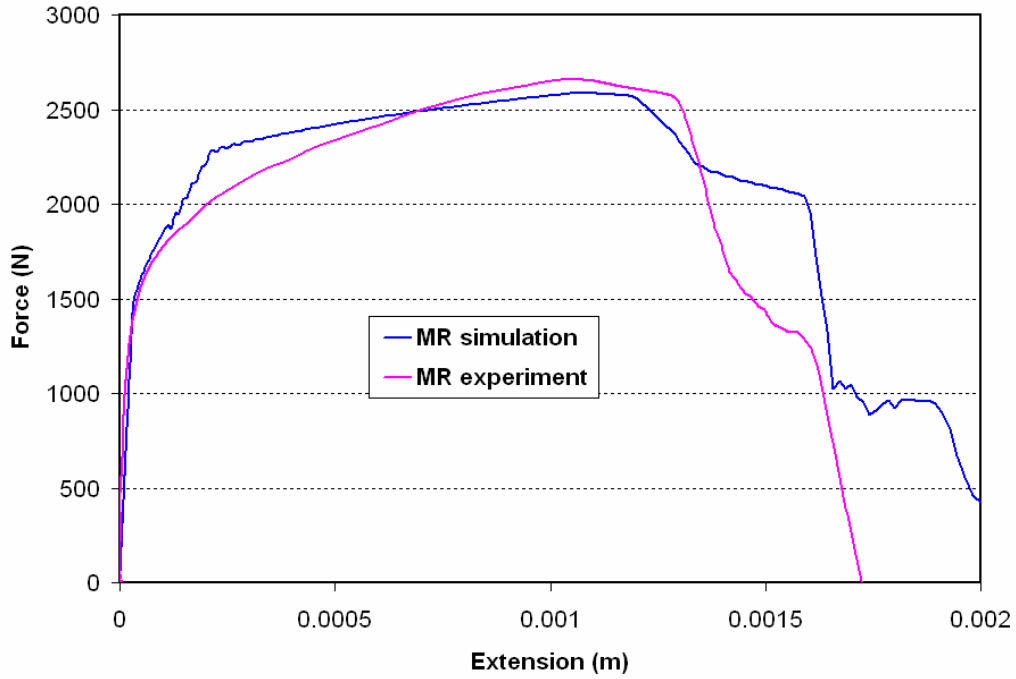


Fig. 2.21 Predicted force extension relationship and the experimental results with rate $\dot{\epsilon} = 100s^{-1}$ in 45-direction

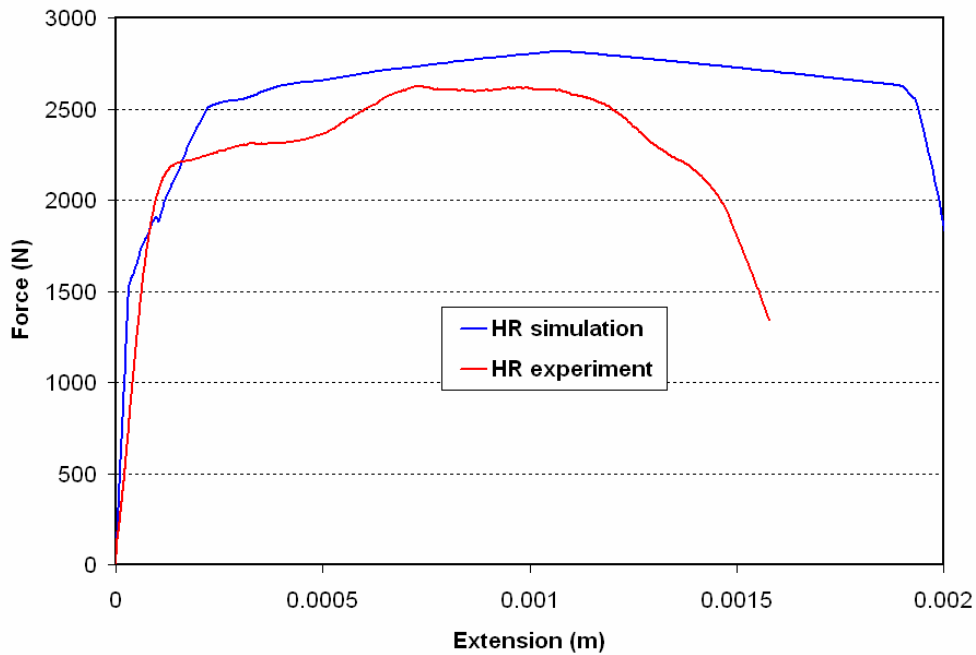


Fig. 2.22 Predicted force extension relationship and the experimental results with rate $\dot{\epsilon} = 3300s^{-1}$ in 45-direction



3 Bird Strike Models

3.1 Bird strike tests to be modelled

Two bird strike tests are to be performed on the Glare ALA wing leading edge structures by CEAT. The only difference between these two tests is the lay-up of the Glare LE skin. As stated in Section 2, the two lay-ups to be used are:

- FML3 4/3 – 0.4 Total thickness = 2.35 mm with lay-up (A/0/90/A/0/90/A/90/0/A)
- FML5 3/2 – 0.4 Total thickness = 2.20 mm with lay-up (A/0/90/0/90/A/90/0/90/0/A)

For both tests, the planned impact angle and impact speed are 0° and 129 m/s respectively.

At the time of preparing this report, it was not decided whether stabilising bars would be used on the outer ribs, to prevent lateral motion of these ribs (as was done for the NLR LE structures – see Fig. 3.1). Thus it was decided to investigate the use of these stabilising bars. Finally, no tests on the rivets being used in this structure are being done in CRAHVI, so no data was available to define a failure law. For that reason, a number of simulations were done to investigate the effect of rivet strength on the response. The full set of simulations performed for this report is listed in Section 4, below.

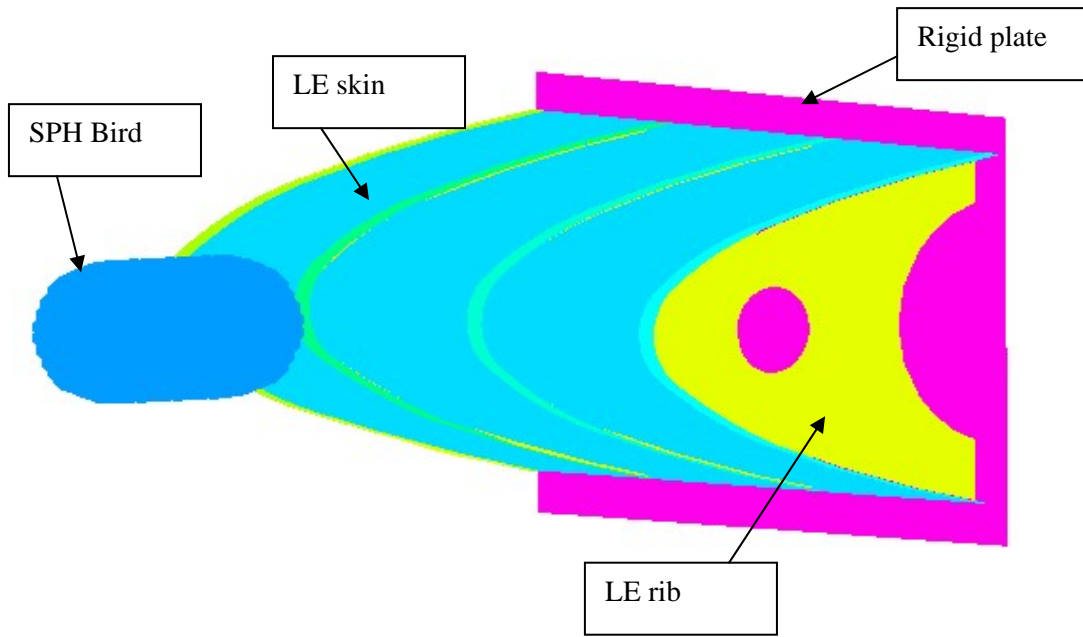


Fig. 3.1 Stabilising Bars used in NLR LE structure tests

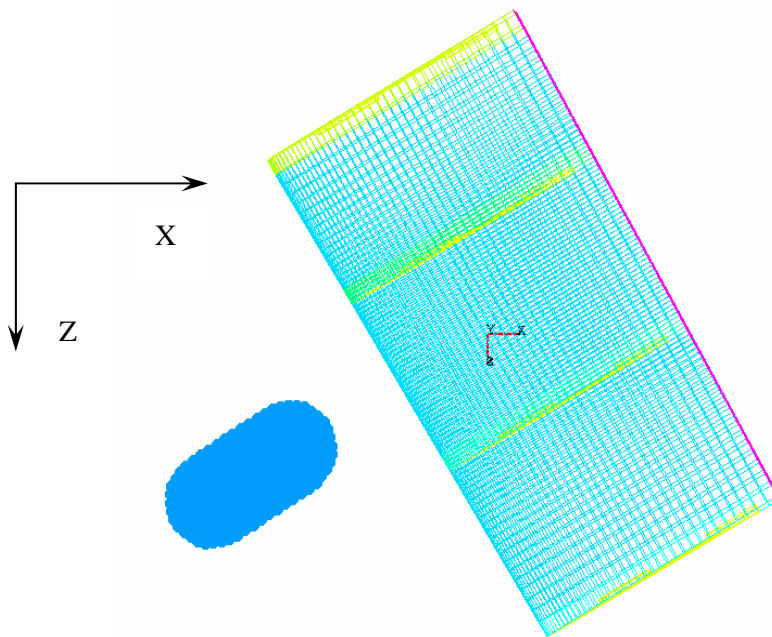
3.2 Finite element model details

A finite element model of the leading edge structure has been created based on the geometry supplied by ALA. This geometry was changed by ALA subsequent to D2.1.3 [3]. The SPH bird model developed by ESI (D1.4.2) was integrated into the model for bird strike simulation as shown in Fig. 3.2. The model contains the SPH bird, one LE skin, four LE ribs with flanges, and a rigid back plate. There are also 125 rivets along the four rib flanges. The rigid back plate simulates the fixture to which the LE structure will be attached during the tests.

In the following sections the finite element model is described in terms of mesh, rivet model, boundary conditions, incorporation of bird model, and material models.



(a) Front perspective view



(b) Top view

Fig. 3.2 SPH Bird with ALA leading edge structure, and coordinate system

3.2.1 FE Meshes

There are in total 8941 elements in the LE model. The LE skin contains 6942 shell elements with mesh edge size between 5 and 19mm as shown in Fig. 3.3. A uniform fine mesh was placed in the impact region between ribs 2 and 3, whereas a coarser mesh was assigned in the regions near rib 1 and rib 4 with a one-way bias.

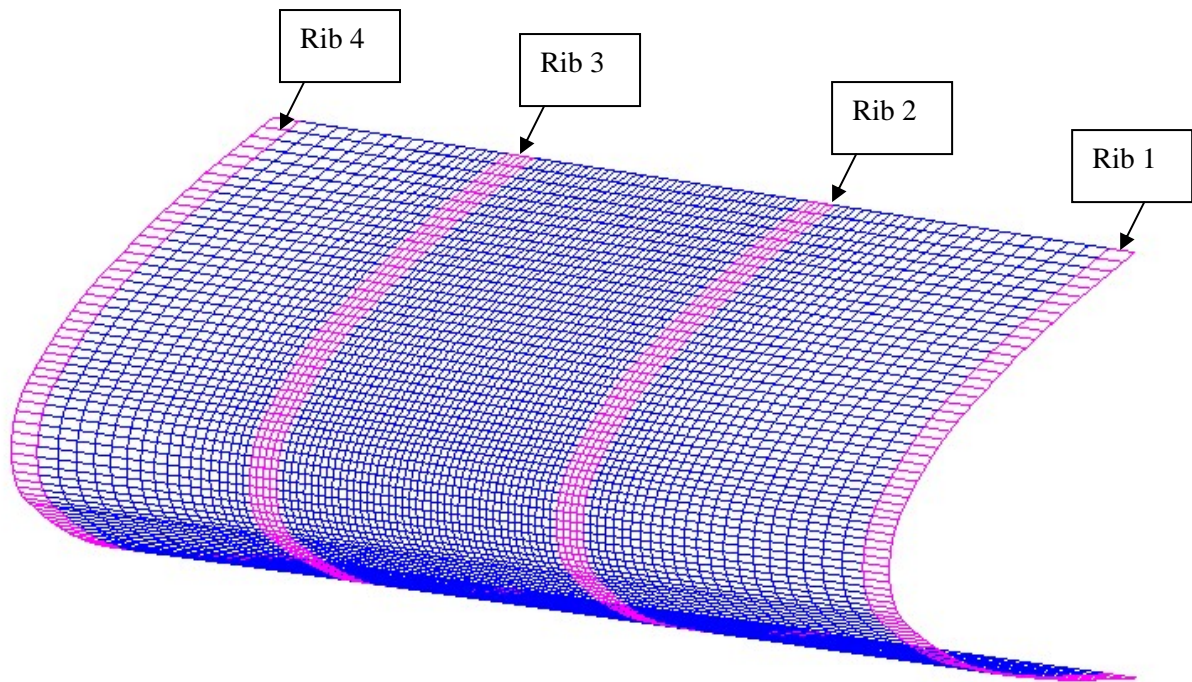


Fig. 3.3 Mesh of LE skin

The LE ribs contain 1422 shell elements with mesh edge size between 6 and 25mm (304 for rib1, 396 for rib2, 398 for rib3 and 324 for rib4) as shown in Fig. 3.4.

Fig. 3.5 gives a closer look at the mesh of the Rib 2. The other ribs have a similar mesh distribution. The rigid plate has 576 shell elements with uniform element size of 20mm as shown in Fig. 3.6.

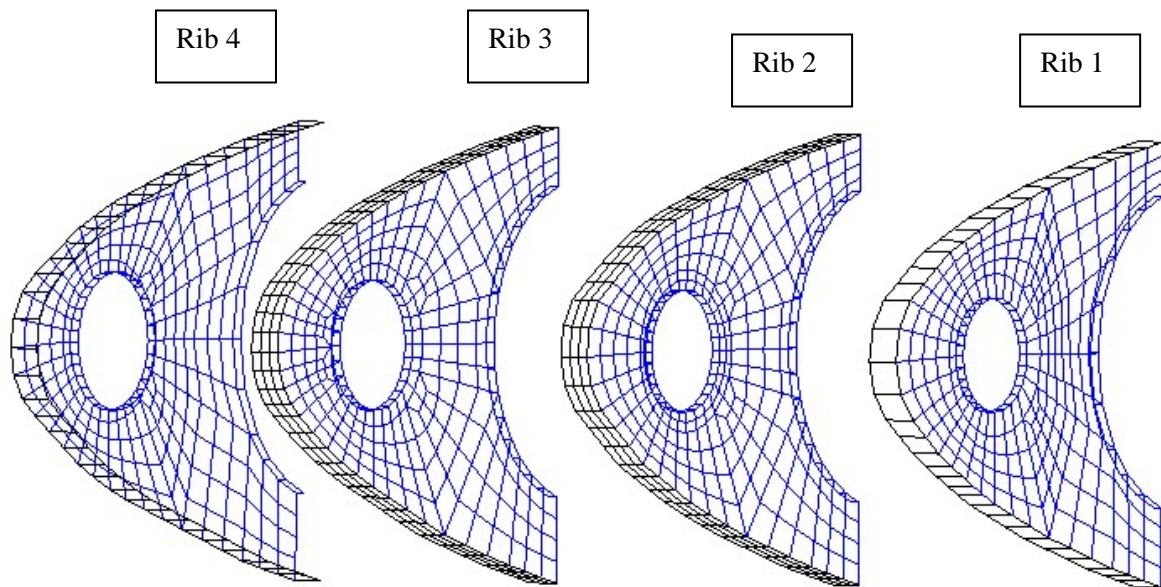


Fig. 3.4 Mesh of LE ribs

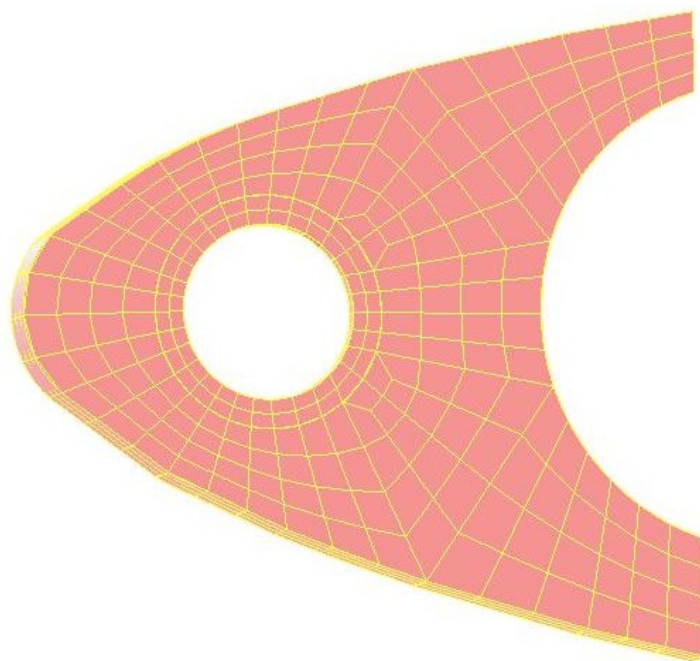


Fig. 3.5 Mesh of Rib 2

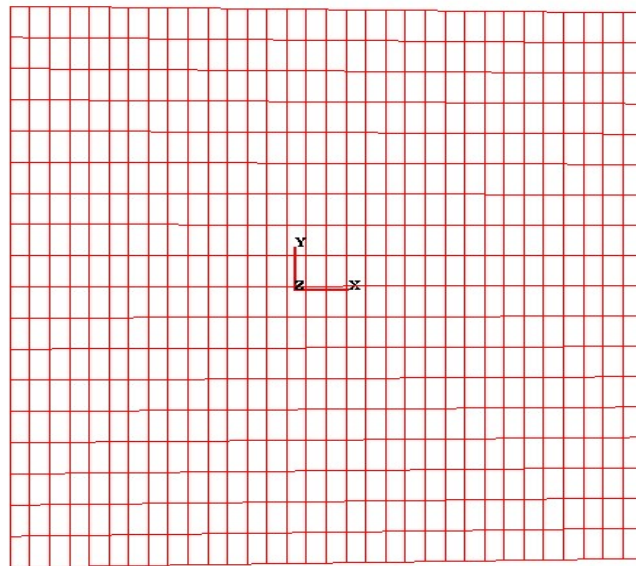


Fig. 3.6 Mesh of the rigid plate

3.2.2 Rivet Modelling

There are 125 rivets distributed along four rib flanges (31 for Rib 1, 30 for Rib 2, 30 for Rib 3, and 34 for rib 4) as shown in Fig. 3.7. The rivets are modelled using mesh-independent rivets/spotwelds (Contact Type 42). This meant that the mesh of the ribs and the skin could be created independently.

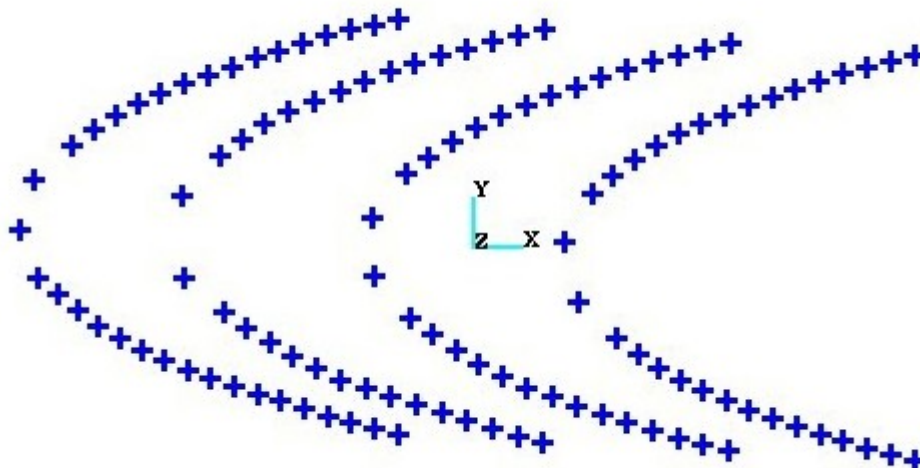


Fig. 3.7 Rivet element in LE model

The rivets used in this structure are of type NASM20426 AD6. They are countersink rivets, made from aluminium alloy 2117-T4 with a nominal diameter of 0.187 inch (4.75mm).

A failure law needed to be introduced to these rivets. Unfortunately, no tests on these rivets are being performed in CRAHVI, so a reasonable estimate had to be made for the failure law. This may be updated in the post-test simulations. It was decided to initially adopt the failure law given in D5.1.2 [12] for rivets made from aluminium alloy 2017, without any changes. The reasons for this are:

- (a) The rivets in [12] were mushroom head while the rivets here are countersunk
- (b) The rivets in [12] were 4mm diameter while the rivets here are 4.75mm

These two effects may oppose each other (countersunk rivets are weaker than mushroom head rivets), so we can guess they might cancel out, making the rivets here similar in strength to those in [12].

From Fig. 12 in D5.1.2, the parameters for the failure law are $N_u = 5100$ newtons, $T_u = 3200$ newtons, $a = 1.5$, $b = 2.1$.

Thus the rivet failure law used initially was:

$$\left(\frac{N}{5100}\right)^{1.5} + \left(\frac{T}{3200}\right)^{2.1} = 1 \quad (3.1)$$

To see the effects of the failure parameters, another simulation was performed with the following failure law:

$$\left(\frac{N}{7200}\right)^{1.5} + \left(\frac{T}{4500}\right)^{2.1} = 1 \quad (3.2)$$

The values of 7200 and 4500 were obtained by multiplying 5100 and 3200 by 1.41 (= $4.75^2/4^2$).

Finally, there is a parameter in the PAM-CRASH rivet rupture law which allows the failure of the rivets to occur over a “failure duration time” rather than instantaneously. This allows some energy-absorption (by plastic deformation of the rivet, or progressive failure of the material) to take place. The effect of this parameter was also investigated.

3.2.3 Boundary Conditions and Contact Interfaces

There are two types of boundary conditions employed in the models: clamping of the skin root and (in one case) stabilising bar connections on the outer ribs, as shown in Figs. 3.8 and 3.9, respectively. The clamped skin root (three rows of nodes, in a region about 30mm from the root, fixed in six degrees of freedom) is used to represent the clamping effect of the



angular plate attached at the skin root. If any deformation of this angular plate occurs in the test, a modified set of boundary conditions will be used in post-test simulations.

Since it was not clear at the time of writing whether stabilising bars would be used, only a very simple approximation to this boundary condition was used, i.e. nine nodes on the outer ribs were fixed in all degrees of freedom. If the bars *are* used, a better model will be incorporated into the post-test simulations.

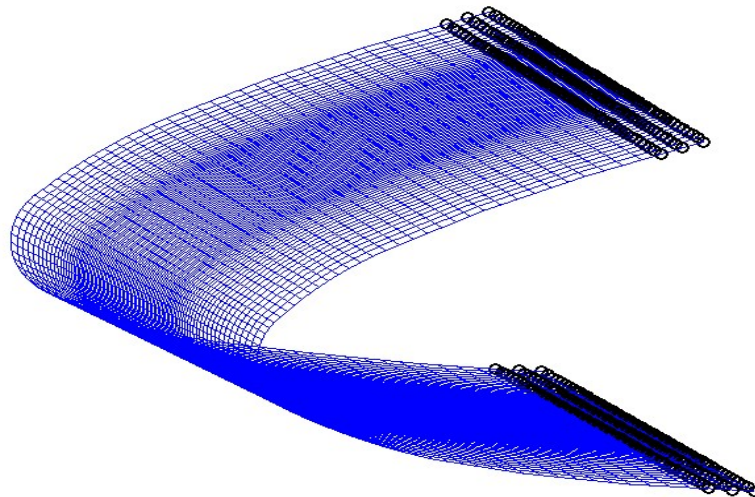


Fig. 3.8 Boundary conditions: clamped skin root

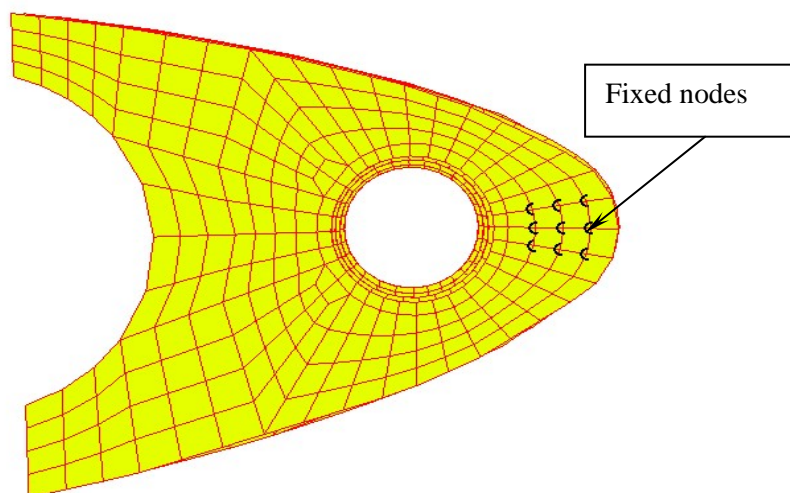


Fig. 3.9 Boundary conditions: stabilising bar connection (rigid for the time being)

There are three types of contact interfaces used in this model:

TYPE 34	used for the bird striking the LE structure, and possible impact between ribs and the rigid plate
TYPE 42	used for simulating the rivet connections
TYPE 36	used for allowing all elements of the structure to contact each other

3.2.4 Incorporation of Bird Model

The original SPH bird provided in D1.4.2 had to be translated and rotated into the right position and impacting angle (as specified by ALA by email) before merging with the LE model. Additionally, the units used in the bird model were metres, and the units in the LE model (Patran file) were millimetres. Thus, the units of the LE model have been scaled into metres.

The vectors for the impacting location and angle are given as (see Fig. 3.2(b) for the global coordinate system):

Location: $[x = 1.86098, y = -0.00506, z = 2.98891]$ in Global Rectangular Coord 0
Impacting direction: $[0.8482, 0.04095, -0.528]$

The positioned SPH bird is shown in Fig. 3.2.

3.2.5 Material Models

The calibrated Glare material model in Section 2 is employed for the skin. The LE ribs are made from aluminium alloy 2024 T3. As mentioned in Section 2, this kind of material does not show much rate dependence (according to [5]), so no strain rate effects are taken into account for this material. The data for this alloy obtained from ESI are adopted for the ribs including the flanges. All material data are shown in Tables 3.2 and 3.3 for ribs and skin, respectively. It should be noted that all PAM-CRASH data in this report is in Version 2002 format.

In Table 3.3 CARD 6 in PART defines the fibre direction where the definition flag '0' indicates that the definition is in terms of the global coordinate system (see Fig. 3.2(b)). The fibre direction obtained from ALA is:

Fibre direction (for 0° layers): $[0.5, 0, 0.866]$

The shear strain limit (more correctly termed the deviatoric strain limit) for element elimination of the rib and skin elements was set to 0.35 and 0.55 respectively.

Table 3.2 Material properties for Ribs

PART /	41SHELL	41						
NAME	From Material 41							
	0.0							
	0.0012							
END_PART								
MATER /	41	105	2700.	0	0	1	0	
	0	0	0	0	0	1.	0	
NAME	Material 41							
	7.240e+10POWER	0.29		0.01	0.01	0.01	0.833333	
	2.7700e+8 4.8500e+8	0.55						
		0	0	0.12	0.21	0.18	0.23	0.9
	0.35		0.0	0.0	0.0	0.0	0.0	0.0



Table 3.3 Material properties for Skin (FML3 Lay-up)

```

$ MATERIAL DATA CARDS
$
$---5---10---5---20---5---30---5---40---5---50---5---60---5---70---5---80
PART /      10SHELL      10
NAME From Material 10 FML3
    0.0

    0.00235
    0          0.5          0          0.866
END_PART
MATER /      10      131          2365.          0          0          1          0
          0          0          0          0          0          0          1.          0
NAME Material 10
    0.0          0.0          10          0.01          0.01          0.01          0.8333
    1 4.0000e-4          0.0
    2 1.2500e-4          0.0
    3 1.2500e-4          90.
    1 4.0000e-4          0.0
    2 1.2500e-4          0.0
    3 1.2500e-4          90.
    1 4.0000e-4          0.0
    3 1.2500e-4          90.
    2 1.2500e-4          0.0
    1 4.0000e-4          0.0
    0.55 100          0
    1 11          1 12          2 11          2 12          3 11          3 12          4 11          4 12
    5 11          5 12          6 11          6 12          7 11          7 12          8 11          8 12
    9 11          9 12          10 11          10 12          0 0          0 0          0 0          0 0
    0 0          0 0          0 0          0 0          0 0          0 0          0 0          0 0
    0 0          0 0          0 0          0 0          0 0          0 0          0 0          0 0
    0 0          0 0          0 0          0 0          0 0          0 0          0 0          0 0
$ PLY 1 : Alu
$
$---5---10---5---20---5---30---5---40---5---50---5---60---5---70---5---80
$
PLY /      1          2          2700.          0          0
NAME Ply 1 : Alu
    7.240e+10POWER          0.29          0.0
    2.7700e+8 4.8500e+8          0.55

          0          0          0.12          0.21          0.18          0.23          0.9
          0.0          0.0          0.0          0.0          0.0

$ Glass Fibre Composite Properties (preliminary calibration)
PLY /      2          1          1550.          0          0
NAME glass fiber; Angle = 0 deg
53.98e+009 9.41e+009
    5.83e+009 5.83e+009          0.28          0.0          0.0
    3500.01 323.944 1700.00 200.00          1.61          480.00          2105.45          0.25
    0.056          0.067          0.99

53.98e+0094.187e-010          0.045          0.048          0.99

    100          0.01          0.01          0.49          0.21
    100          0.22          0.14          0.32          0.11
    
```



The material properties for the SPH bird, shown in Table 3.4, were those provided by ESI in D1.4.2 [2], with the following modifications following advice from ESI:

- A cut-off pressure of -1000 is added
- The anti-crossing force parameter has been changed from 0.1 to 0.01

Table 3.4 Material properties for the SPH bird

```

$ MATERIAL DATA CARDS
$
$---5---10---5---20---5---30---5---40---5---50---5---60---5---70---5---80
PART /      1SPHEL      1
NAME From Material 1
      0.0

      2.      0.01      0.015      0.01      0      0
END_PART
MATER /      1      28      962.      0      0      1      0
      0      0      0      0      0      0      1.      0
NAME Material 1
      1.2800e+8      7.98
      0.0      -1000
    
```

4 Results and Discussion

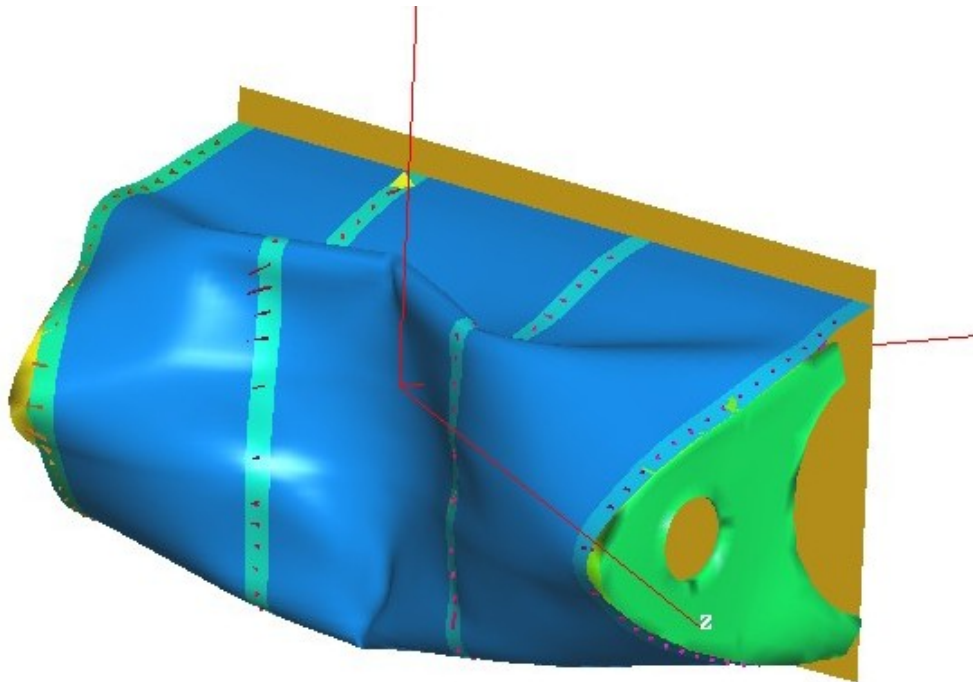
In total seven simulations, as shown in Table 4.1, are presented here. The first four were carried out using the FML3 lay-up, with four different rivet failure laws. The fifth used one of these rivet failure laws and added stabilising bars on the outer ribs. The sixth and seventh were for the FML5 lay-up with two different rivet failure laws.

Table 4.1 Birdstrike simulation cases performed for this report

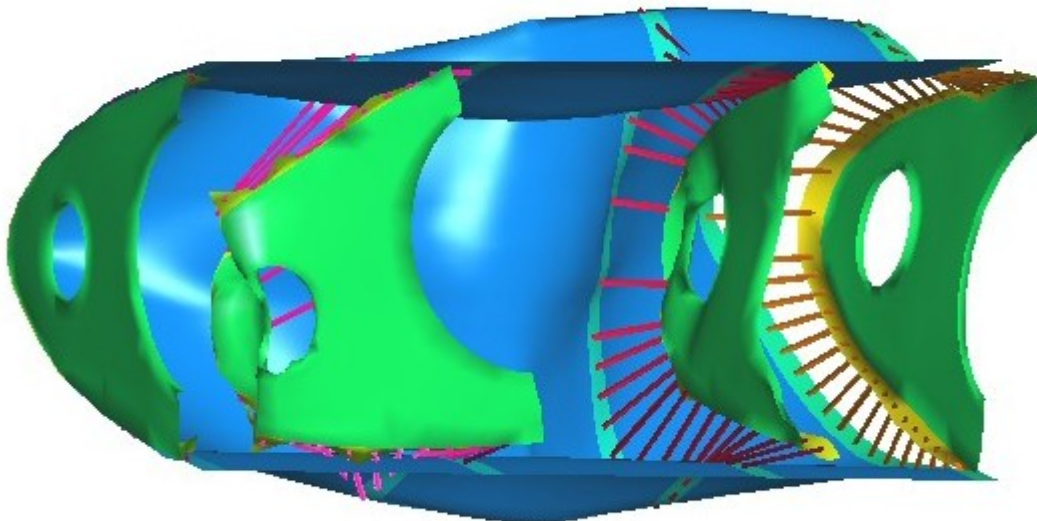
Simulation Number	Simulation ID	Glare Material	Stabilising Bars Used	Rivet failure law
1	FML3_Law1_0ms	FML3	No	Eqn (3.1)
2	FML3_Law2_0ms	FML3	No	Eqn (3.2)
3	FML3_Law1_1ms	FML3	No	Eqn (3.1) with failure duration 1 ms
4	FML3_NoFailure	FML3	No	No failure
5	FML3_Law1_1ms_Bars	FML3	Yes	Eqn (3.1) with failure duration 1 ms
6	FML5_Law1_1ms	FML5	No	Eqn (3.1) with failure duration 1 ms
7	FML5_NoFailure	FML5	No	No failure



The results of the first four cases show the influence of the rivet failure law on the response of the structure. The final state in both front view and rear view of the four cases are presented in Figs. 4.1 - 4.4, respectively.

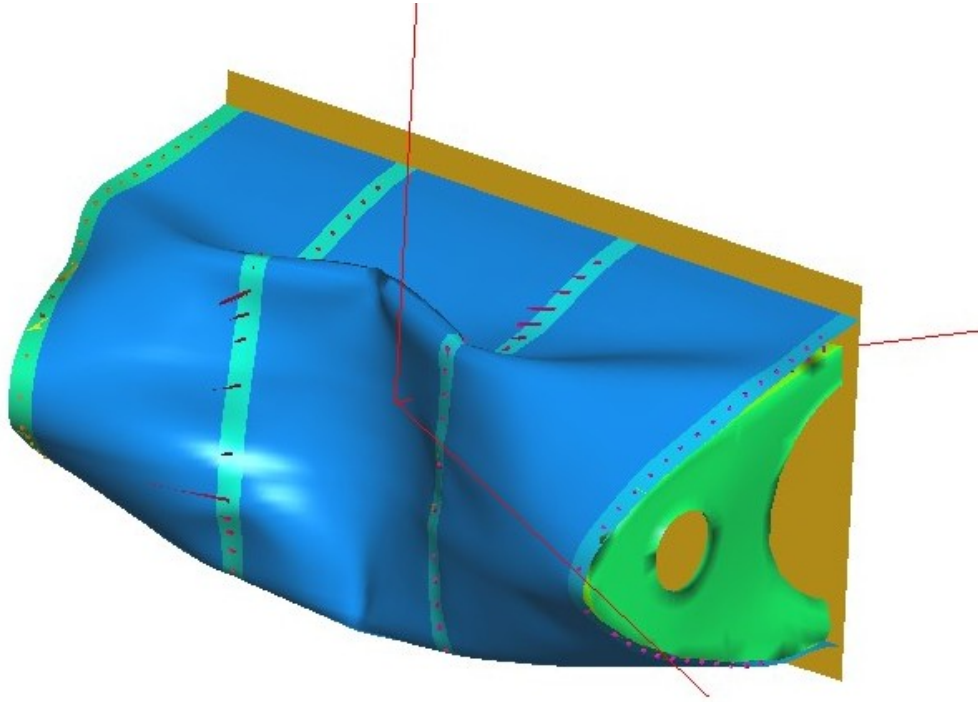


(a) Front view

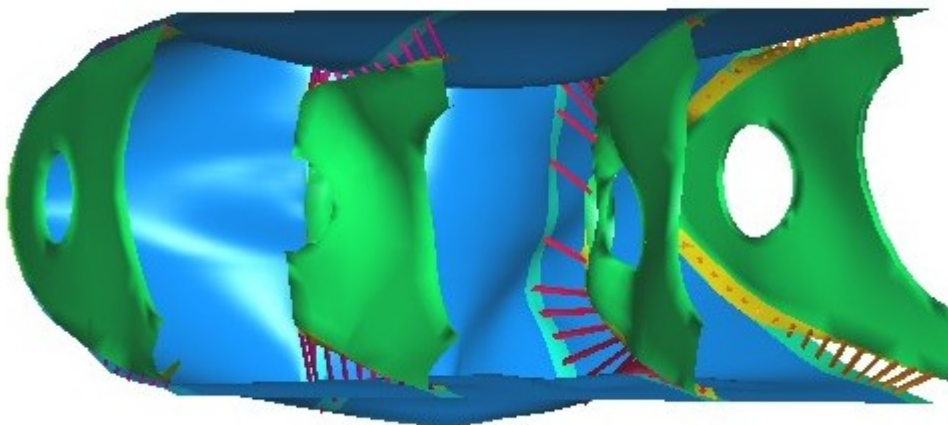


(b) Rear view

Fig. 4.1 The final state of FML3_Law1_0ms (Rivet failure law: equation 3.1 with 0ms failure duration)

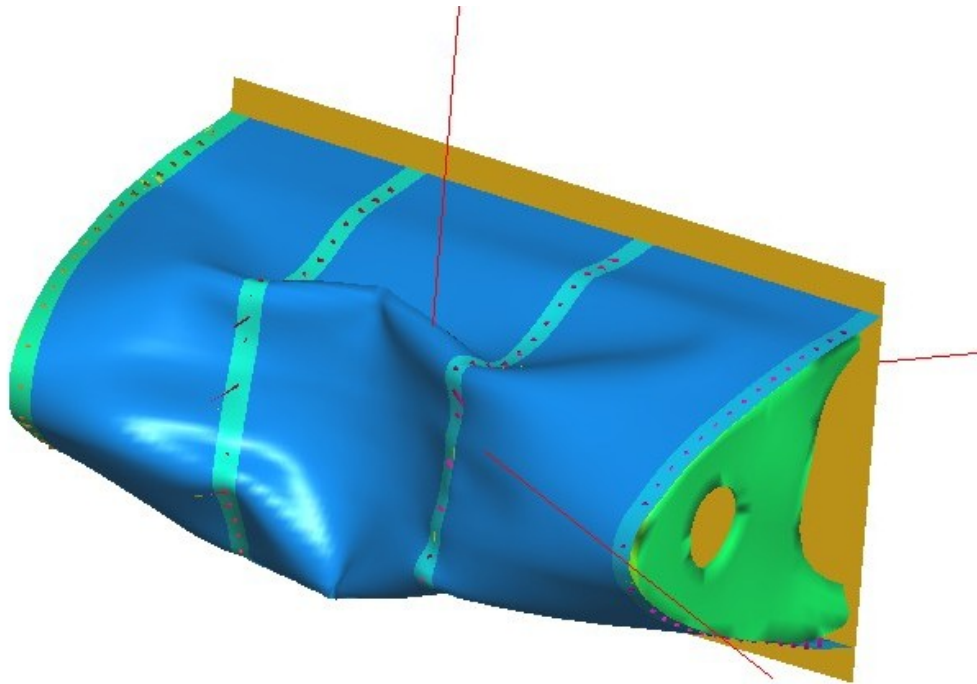


(a) Front view

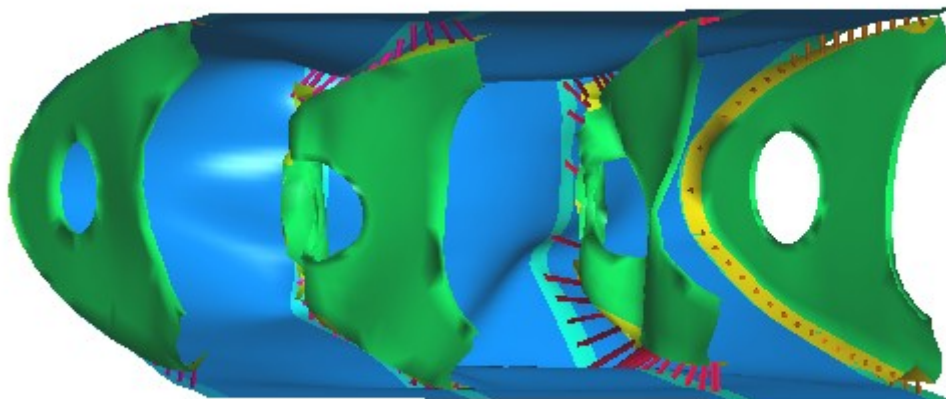


(b) Rear view

Fig. 4.2 The final state of FML3_Law2_0ms (Rivet failure law: equation 3.2 with 0ms failure duration)

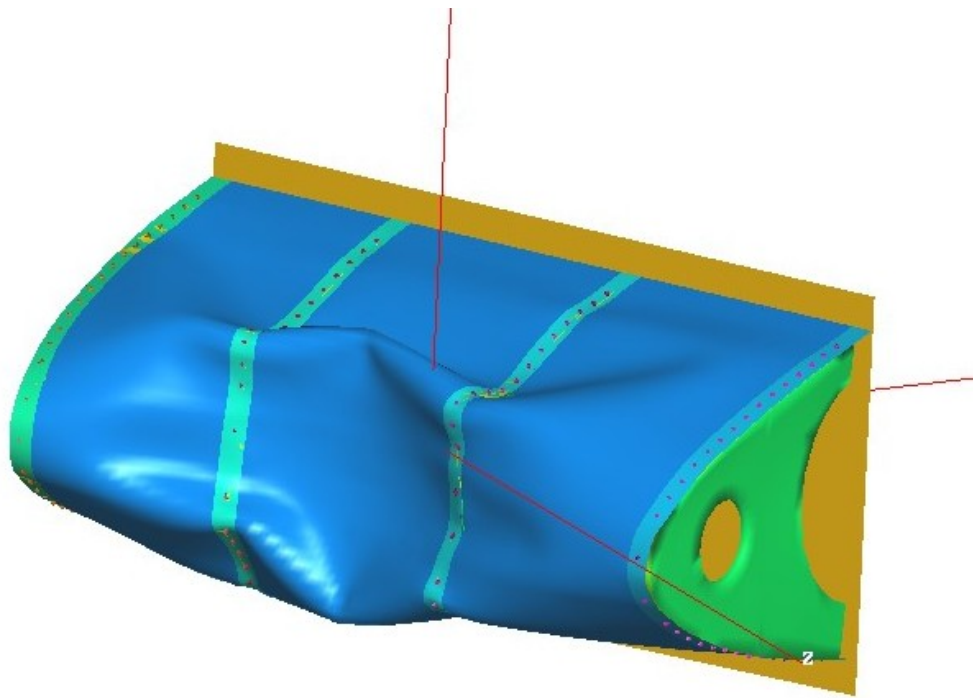


(a) Front view

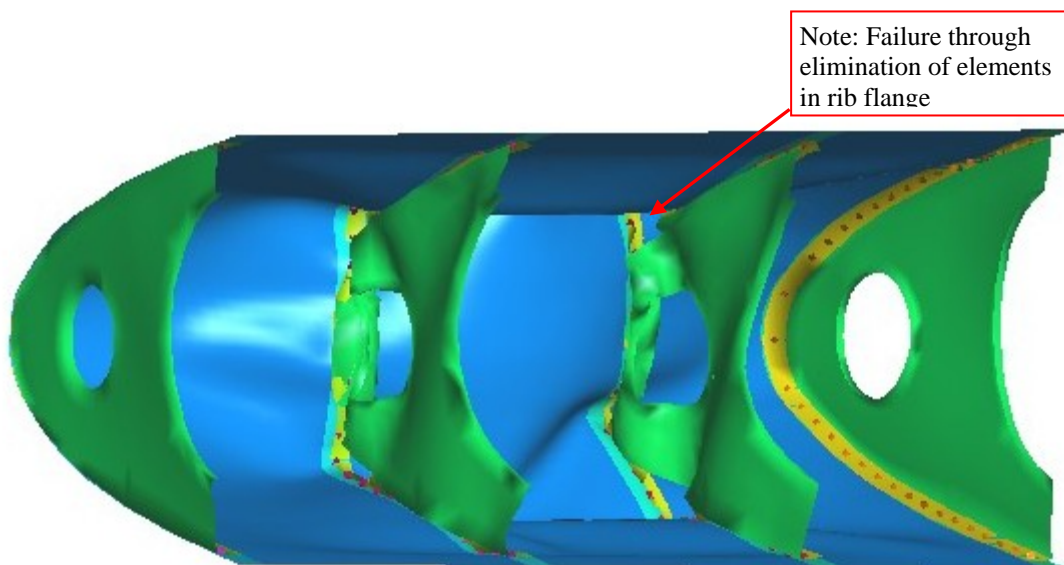


(b) Rear view

Fig. 4.3 The final state of FML3_Law1_1ms (Rivet failure law: equation 3.1 with 1ms failure duration)



(a) Front view



(b) Rear view

Fig. 4.4 The final state of FML3_NoFailure (no rivet failure law)

From Figs. 4.1 - 4.4, one can see that the rivet failure law has a large influence on the response of the LE structure. An interesting feature in Fig. 4.4 is that even with no rivet failure allowed there is separation of the skin and rib near the front of the rib, through elimination of elements in the rib flange. This gives an indication of the strength of the forces trying to cause separation at this location, and indicates that rivet failure or pull-through here is highly likely.

The deformation of the structure for these four cases is shown in Fig. 4.5. The curves are in fact the displacement of node 307712 (see Fig. 4.6). Clearly, FML3_NoFailure provides the lower bound, while FML3_Law1_0ms gives the upper bound from among the cases studied. Increasing the failure duration to 1ms has significantly more effect on the maximum displacement than increasing the rivet failure loads to those in equation 3.2.

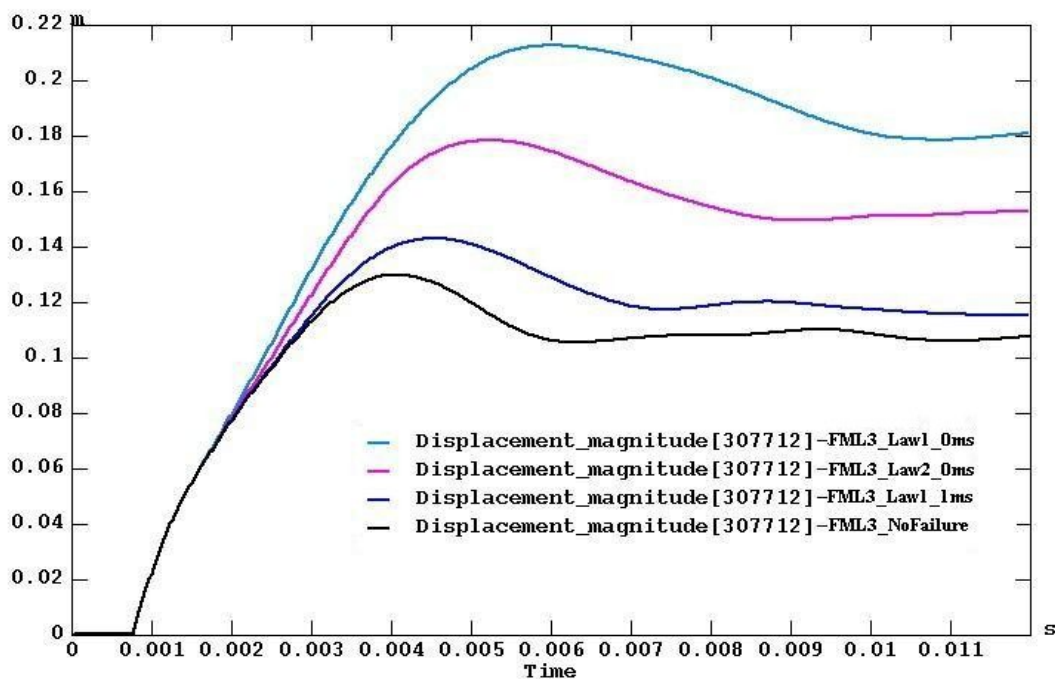


Fig. 4.5 Deformation of LE structure with FML3 lay-up, no stabilising bars and four different rivet failure laws



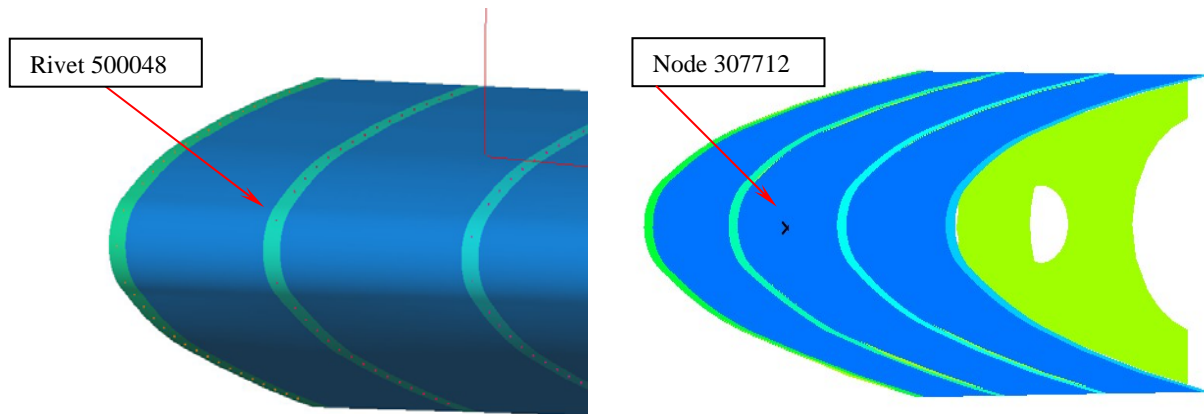


Fig. 4.6 Location of rivet 500048 and Node 307712

To better understand the influence of the rivet failure laws, the normal force vs time and shear force vs time are plotted for rivet 500048 (see Fig. 4.6 for the location of this rivet) in Figs. 4.7 and 4.8, respectively. It can be seen that in even in the no_failure case, the rivet force drops to very low levels at around 2.7ms, due to the elimination of rib flange elements noted above. Increasing the rivet normal and shear failure strengths has little effect since the high rivet forces are experienced for such a short time – the failure is seen to be dominated by the shear force. Finally, increasing the failure duration is seen to be much more influential in terms of the energy absorbed by the rivet, and the behaviour approaches that of the no-failure case. Though it is impossible to say at this point, we regarded the FML3_Law1_1ms (i.e. equation 3.1 with a failure duration of 1ms) as possibly the most realistic prediction, and for this reason used this law in later simulations which included the effects of stabilising bars and also the effect of changing the lay-up.

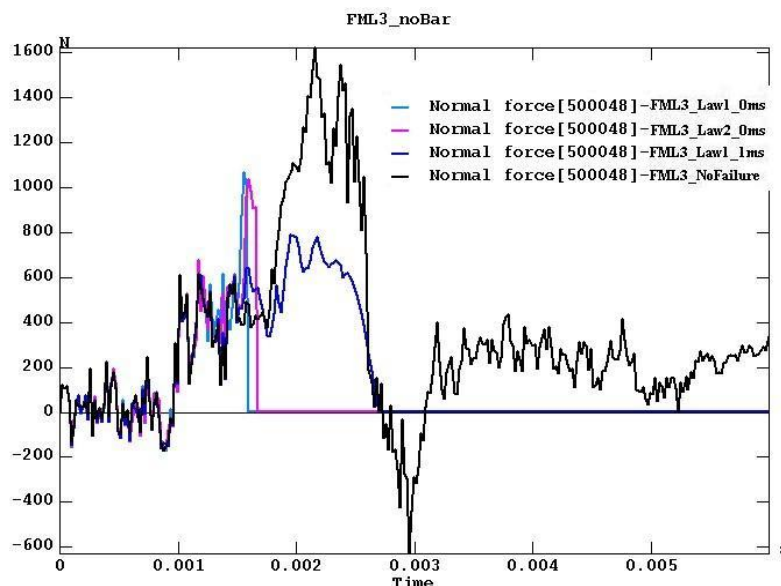


Fig. 4.7 Normal force in Rivet 500048

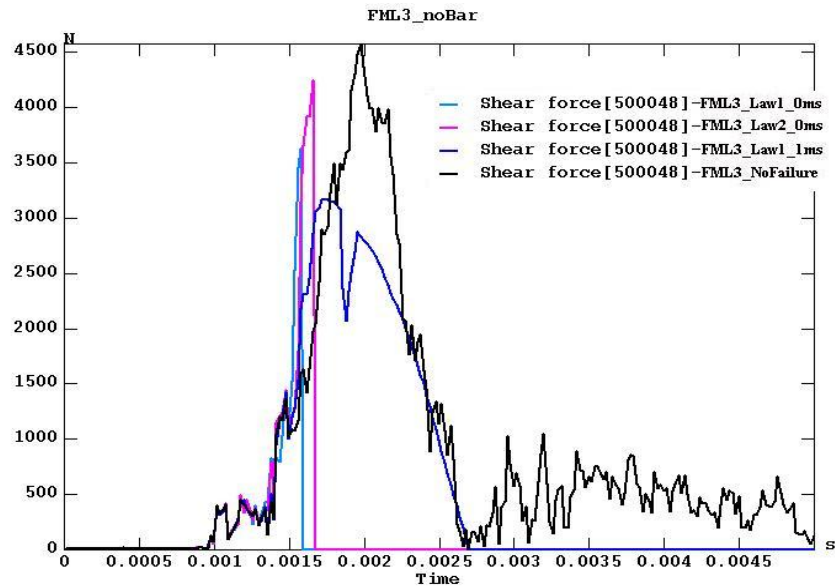


Fig. 4.8 Shear force in Rivet 500048

The deformation histories of the bird and the LE structure in the FML3_Law1_1ms case are shown in Figs. 4.9 and 4.10 respectively. In Figs. 4.11 – 4.14, the damage and (for the aluminium layer) plastic strain in the skin are shown for layers 1, 2, 3, and 5. As a reminder, the lay-up in this case is A/0/90/A/0/90/A/90/0/A. Large plastic strains exist at localised regions in the aluminium layers. This is because of the use of damage parameters in the aluminium alloy material properties (see Table 2.2). Once the plastic strain reaches 23%, the damage is set to its ultimate value of 0.9, which means that plastic strain can proceed from this point with very little resistance. The difference in the damage pattern in the 0° and 90° composite layers is apparent and seems to be reasonable. The damage in Layer 5 is considerably less than in Layer 2, which is reasonable since Layer 5 is an interior layer, and hence sees lower bending stresses.

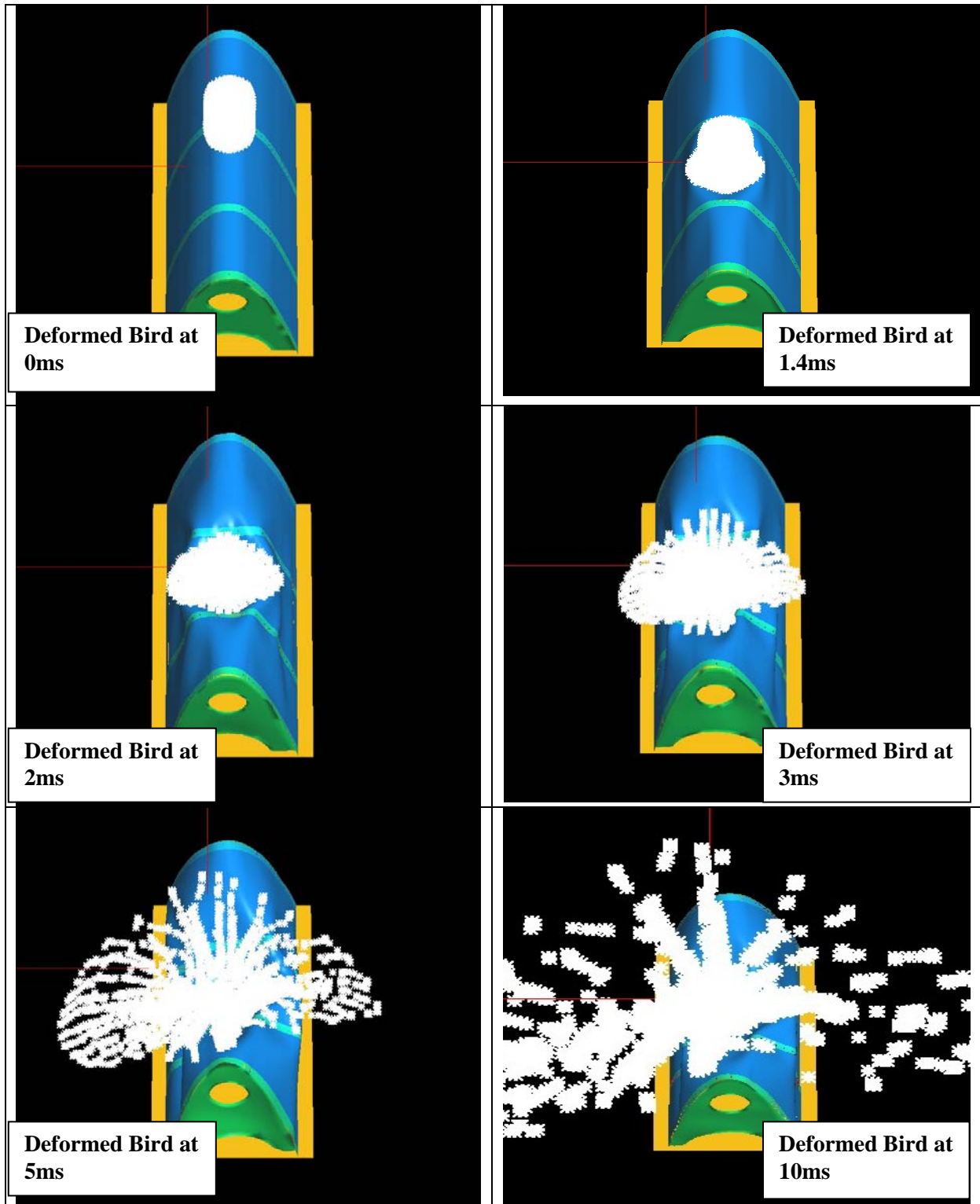


Fig. 4.9 Deformed shape of the Bird in FML3_Law1_1ms

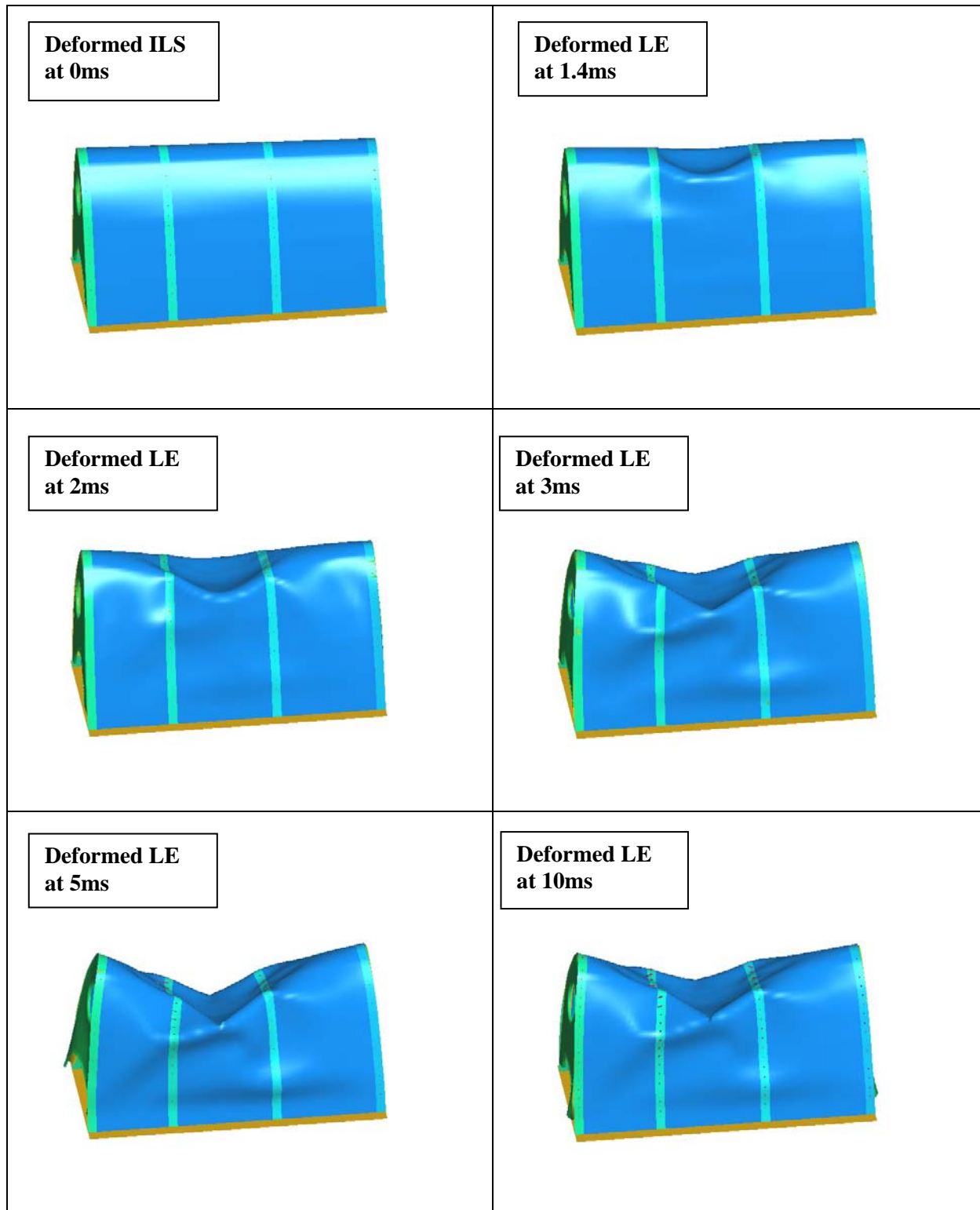
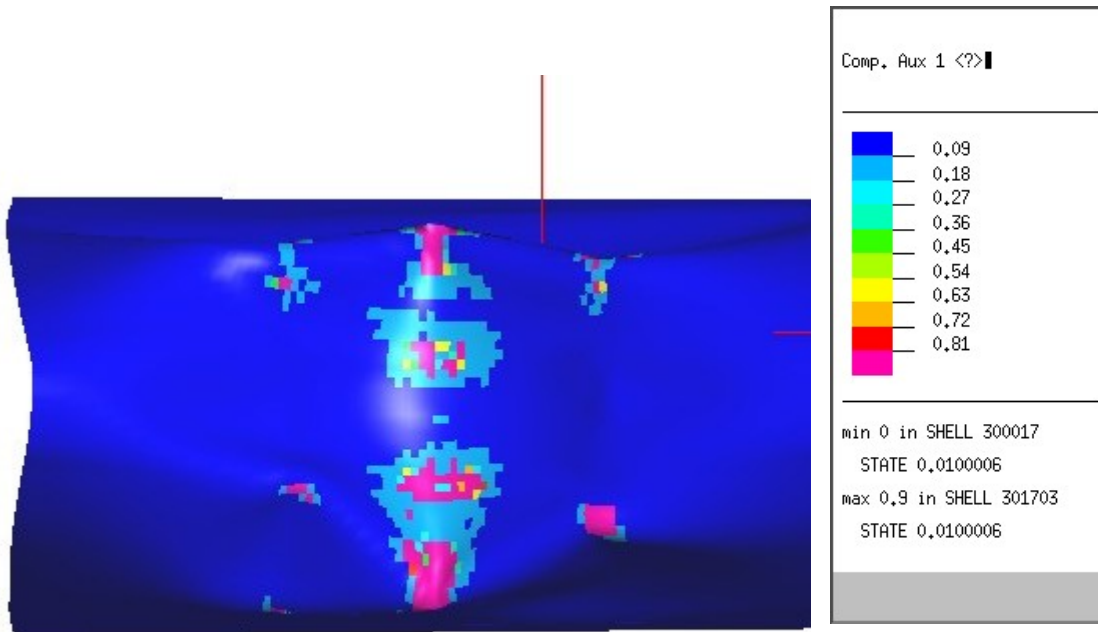
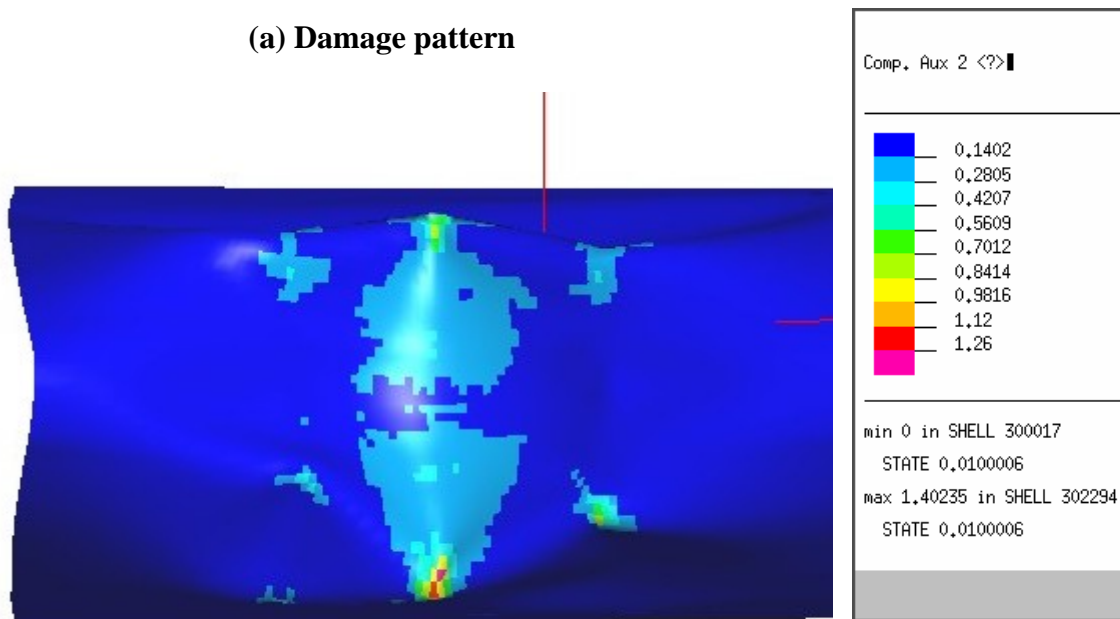


Fig. 4.10 Deformation history of the LE structure with FML3_Law1_1ms

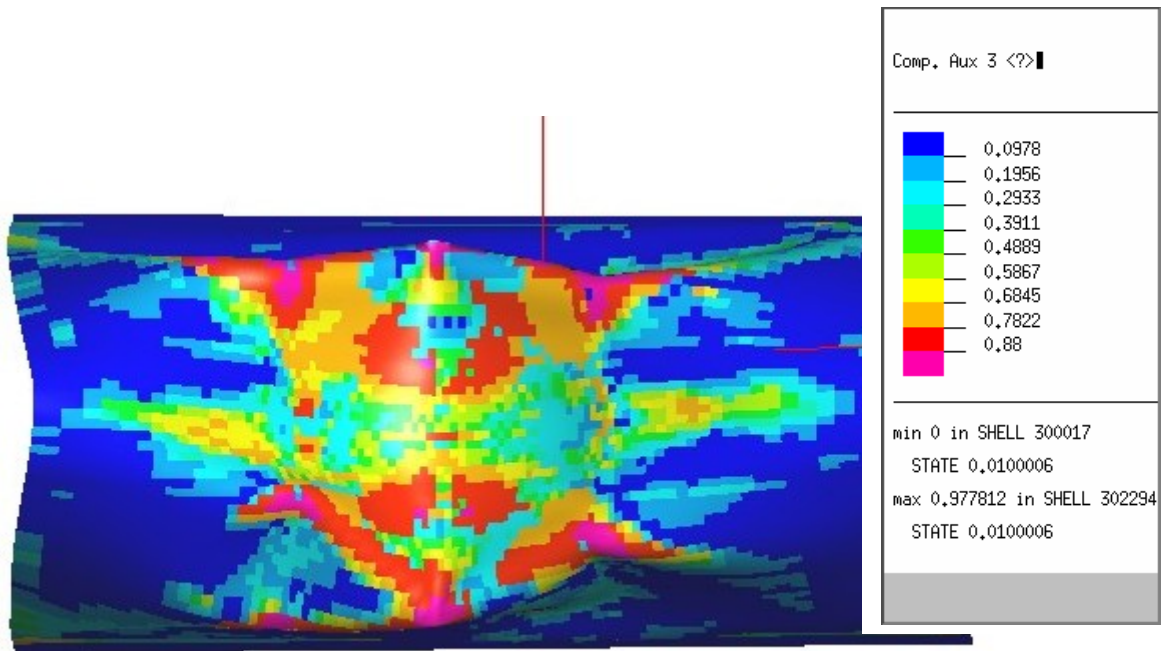


(a) Damage pattern

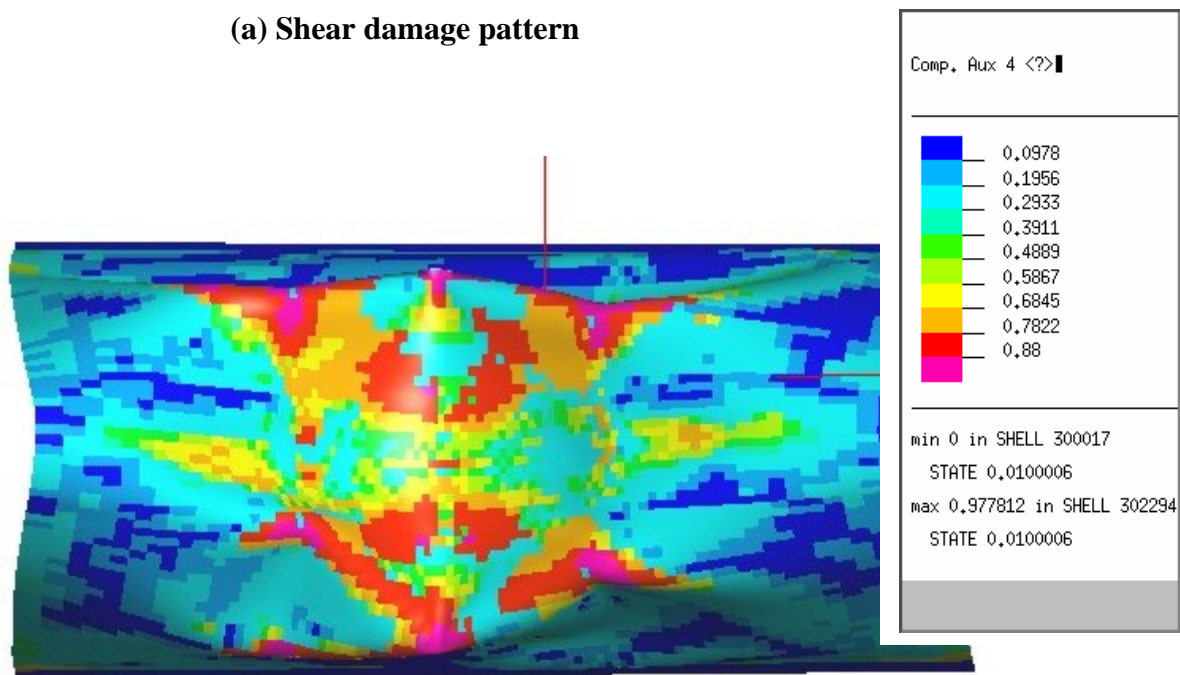


(b) Plastic strain pattern

Fig. 4.11 Damage and plastic strain in the LE skin at the final state of FML3_Law1_1ms (LAYER 1: Aluminium)

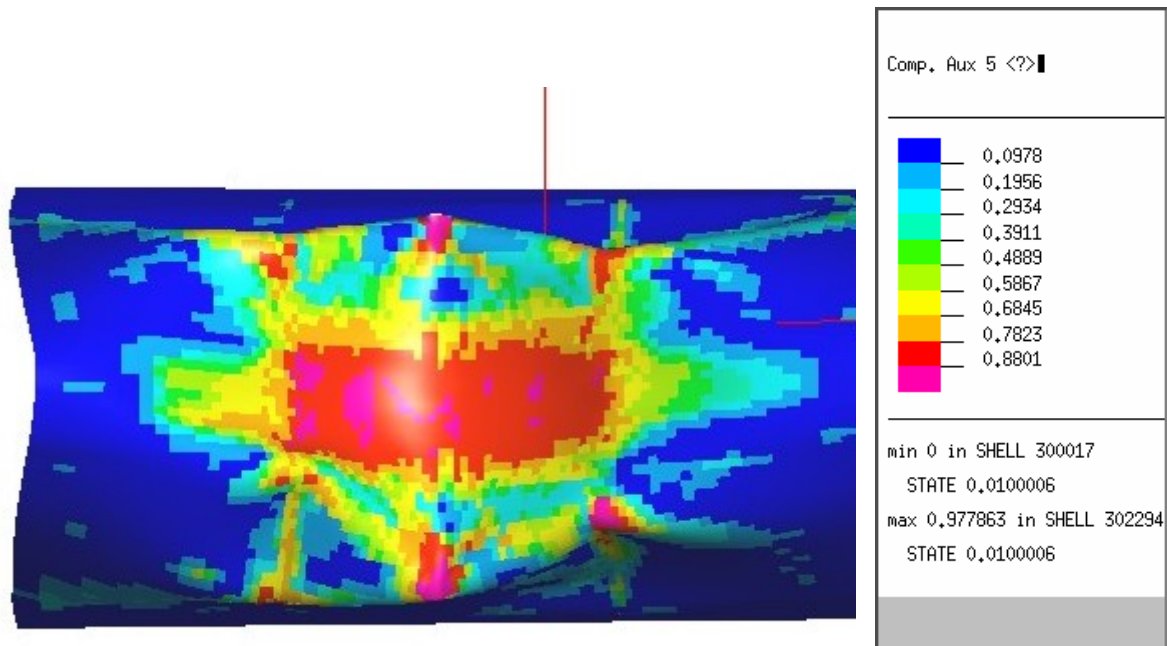


(a) Shear damage pattern

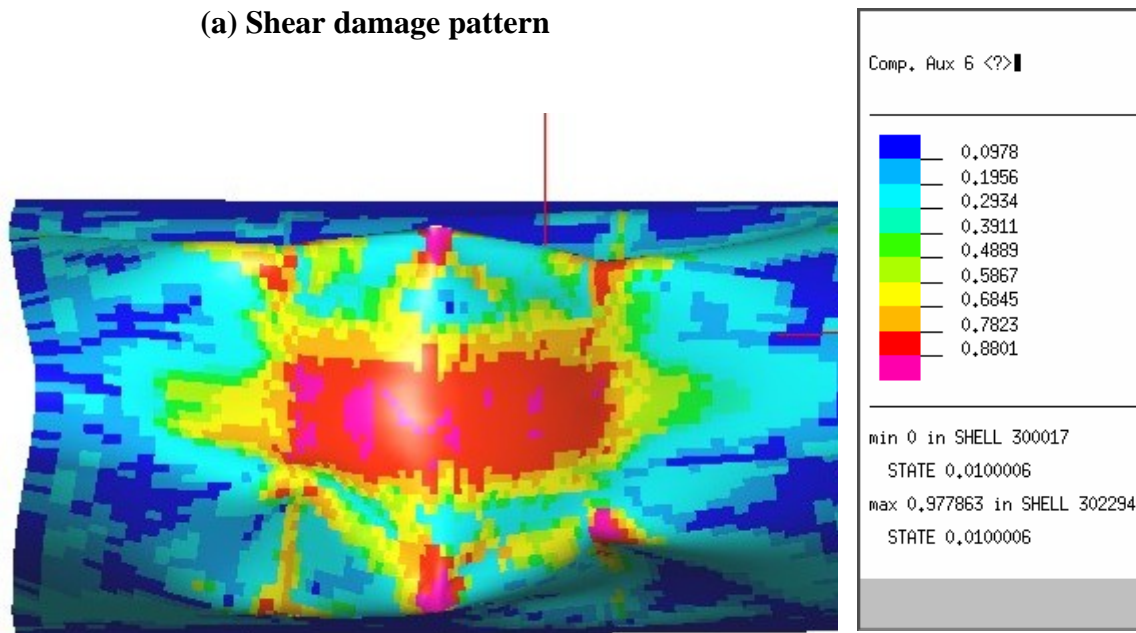


(b) Transverse damage pattern

**Fig. 4.12 Damage in the LE skin at the final state of FML3_Law1_1ms
(LAYER 2: 0 degree Composite)**

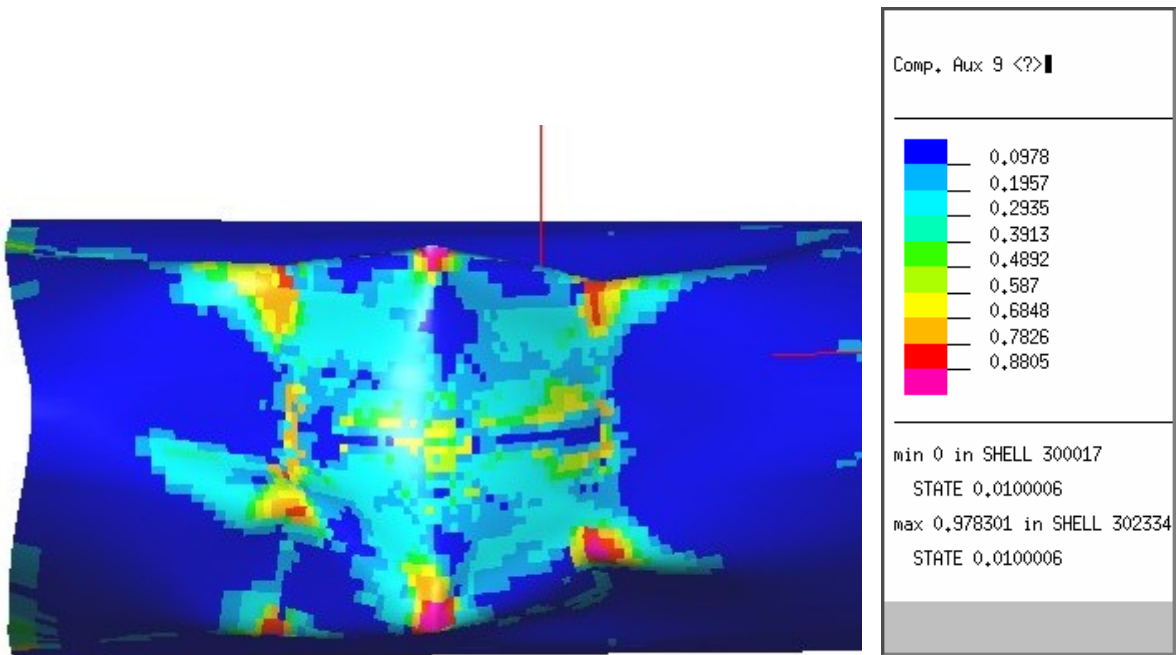


(a) Shear damage pattern

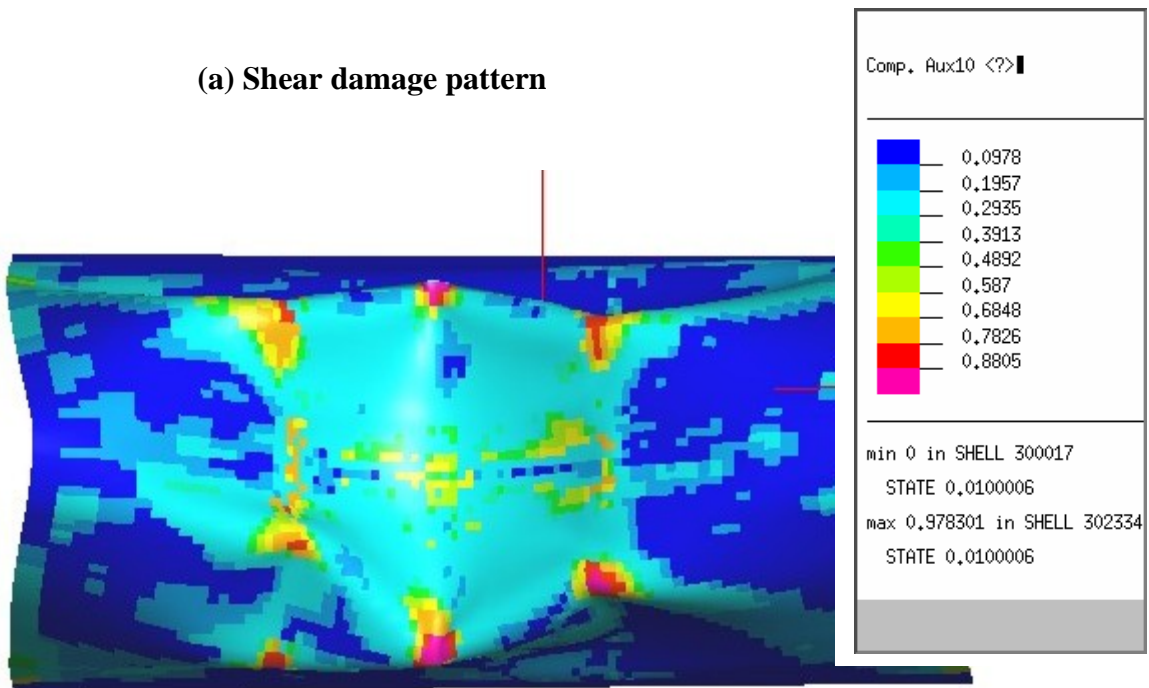


(b) Transverse damage pattern

**Fig. 4.13 Damage in the LE skin at the final state of FML3_Law1_1ms
(LAYER 3: 90 degree Composite)**



(a) Shear damage pattern



(b) Transverse damage pattern

**Fig. 4.14 Damage in the LE skin at the final state of FML3_Law1_1ms
(LAYER 5: 0 degree Composite)**

The effects of stabilising bars are studied in Figs. 4.15 - 4.18. In these two cases, the lay-up was FML3 and the rivet failure law was equation 3.1 with 1ms failure duration.

From Figs 4.15 and 4.17, *without* bars, Rib 4 has lateral movement of 43mm while Rib 1 moves laterally only 19mm (at the locations to which the bars would be connected). Thus Rib 4 has by far the greater tendency to move laterally.

Fig. 4.16 shows that the bars prevent the ribs from moving in, but not the skin, since rivet failure occurs. Fig. 4.18 confirms that the maximum deformation of the skin (i.e. of node 307712 – see Fig. 4.6) is not much affected by the bars. Thus the prediction here is that the bars should not make much difference, but of course if the rivets do not fail on the outer ribs, this prediction would be wrong.

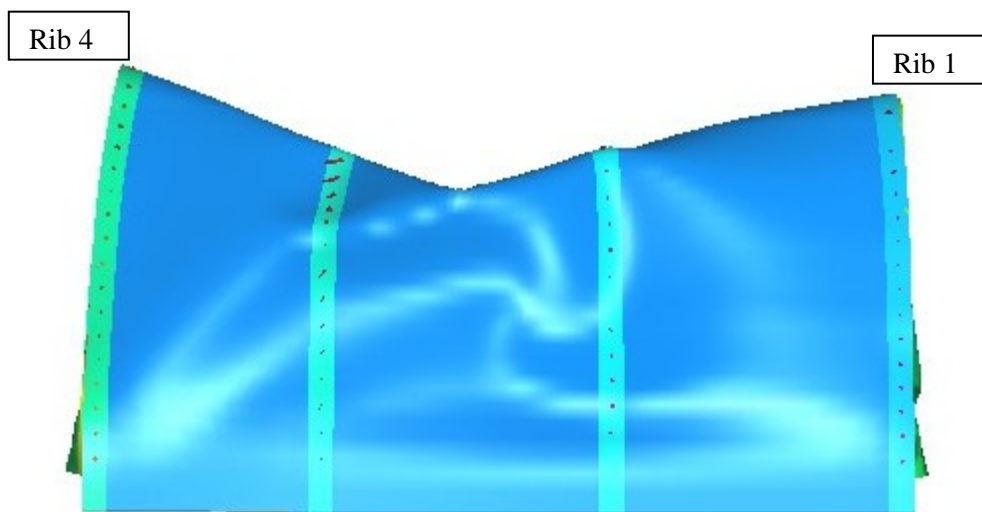


Fig. 4.15 Lateral movements in Ribs 1 and 4 in the LE structure WITHOUT stabilising bars (FML3_Law1_1ms)

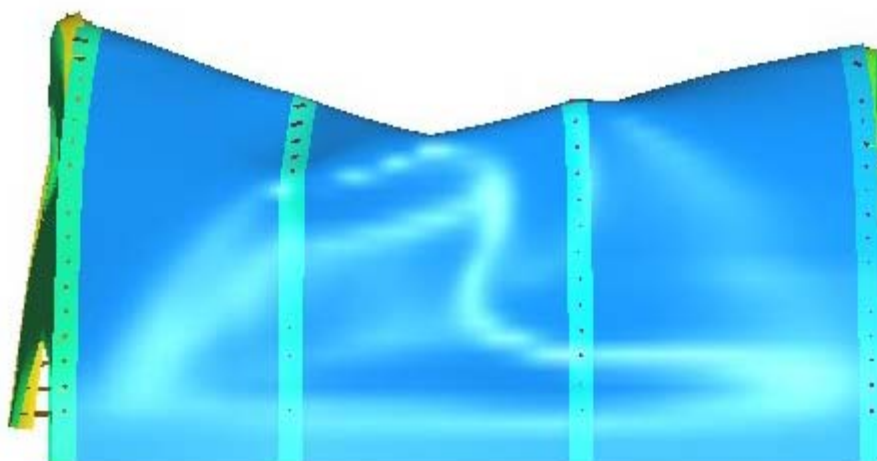


Fig. 4.16 Lateral movements in Ribs 1 and 4 in the LE structure WITH stabilising bars (FML3_Law1_1ms_bars)

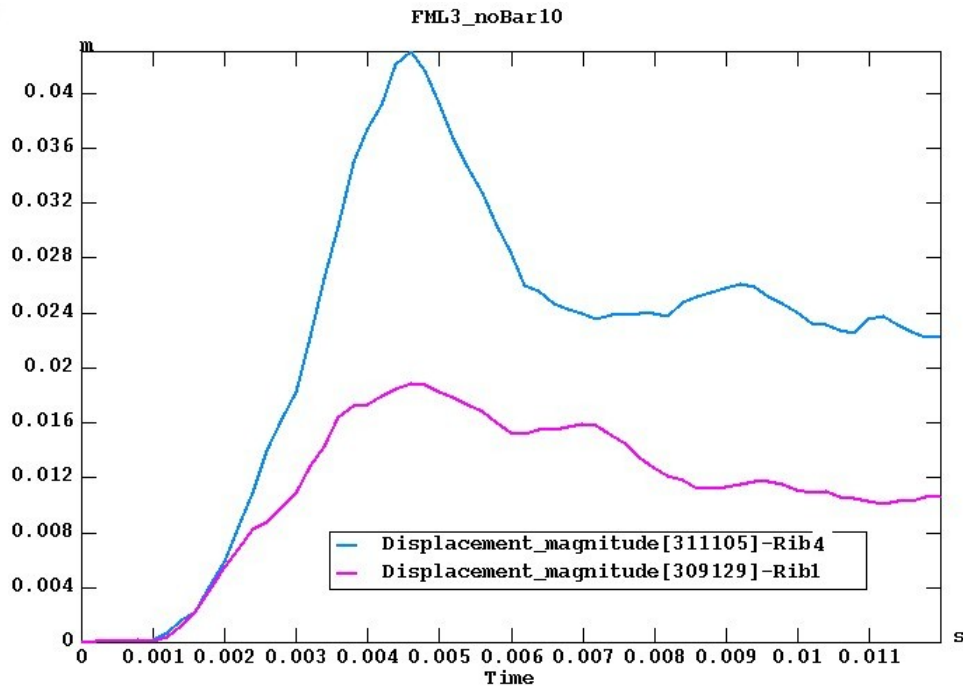


Fig. 4.17 Lateral displacements at Rib 1 and Rib 4 of the LE structure WITHOUT stabilising bars (FML3_Law1_1ms)

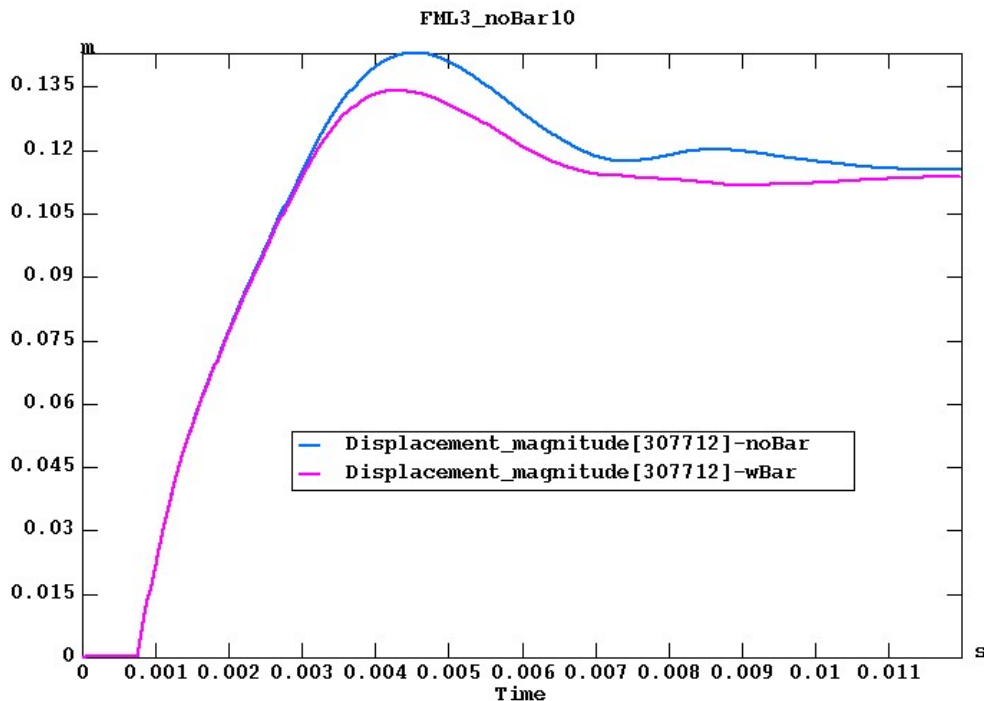


Fig. 4.18 Displacements of node 307712 of the LE structures with/without stabilising bars (FML3_Law1_1ms, and FML3_Law1_1ms_Bars)



The results for the FML5 lay-up are presented next. The deformation histories of the bird and the LE structure in the FML5_Law1_1ms case (i.e. no stabilising bars, with rivet failure law given by equation 3.1, with 1ms failure duration) are shown in Figs. 4.19 and 4.20 respectively. In Figs. 4.21 – 4.24, the damage and (for the aluminium layer) plastic strain in the skin are shown for layers 1, 2, 3, and 6. As a reminder, the lay-up in this case is A/0/90/0/90/A/90/0/90/0/A. There is thus a larger proportion of glass to aluminium layers in FML5 than there was in FML3. Finally, in Fig. 4.25 the deformation of the skin is shown for FML5 and FML3 with and without a rivet failure law. All results are summarised in Table 4.2.

From Fig. 4.20 and 4.25, the FML5 specimen clearly undergoes larger deformation than the FML3 specimen, whether or not rivet failure is allowed. This result would be predicted from a consideration of the *quasi-static* properties of the constituent materials of Glare, since a higher proportion of glass should lead to a less stiff structure. However, since the calibration used here assumed that the glass layers increased their strength at high strain rates, there was the possibility that this could make the deformation of FML5 *less* than FML3 under dynamic loading. This was not the case. Another interesting feature of Fig. 4.25 is the greater rebound of the displacement in the FML5 cases, compared to the FML3 cases. This is because plastic deformation was not included in the material model used for the composite layers, whereas it was for the aluminium layers. The lay-up with the larger percentage of aluminium (FML3) shows the most plastic (i.e. non-recoverable) deformation.

The damage patterns in Figs. 4.21 – 4.24 are similar to those in the FML3 case. The damage in the central aluminium layer (Layer 6) is clearly less than in the outer aluminium layer (Layer 1), as would be expected since the interior layers see less bending stress than the outer layers.

Finally, Table 4.2 shows the high number of rivets that are predicted to fail (considering only 125 rivets exist in the model) in all the cases that allow rivet failure. Whether this is realistic or not is unknown. Most likely, partial (bearing) failures will occur at most rivets, while the number that actually fail completely may be considerably less than shown in the table. Rivet failure near the front of Ribs 2 and 3 is considered highly likely for the reasons stated earlier.

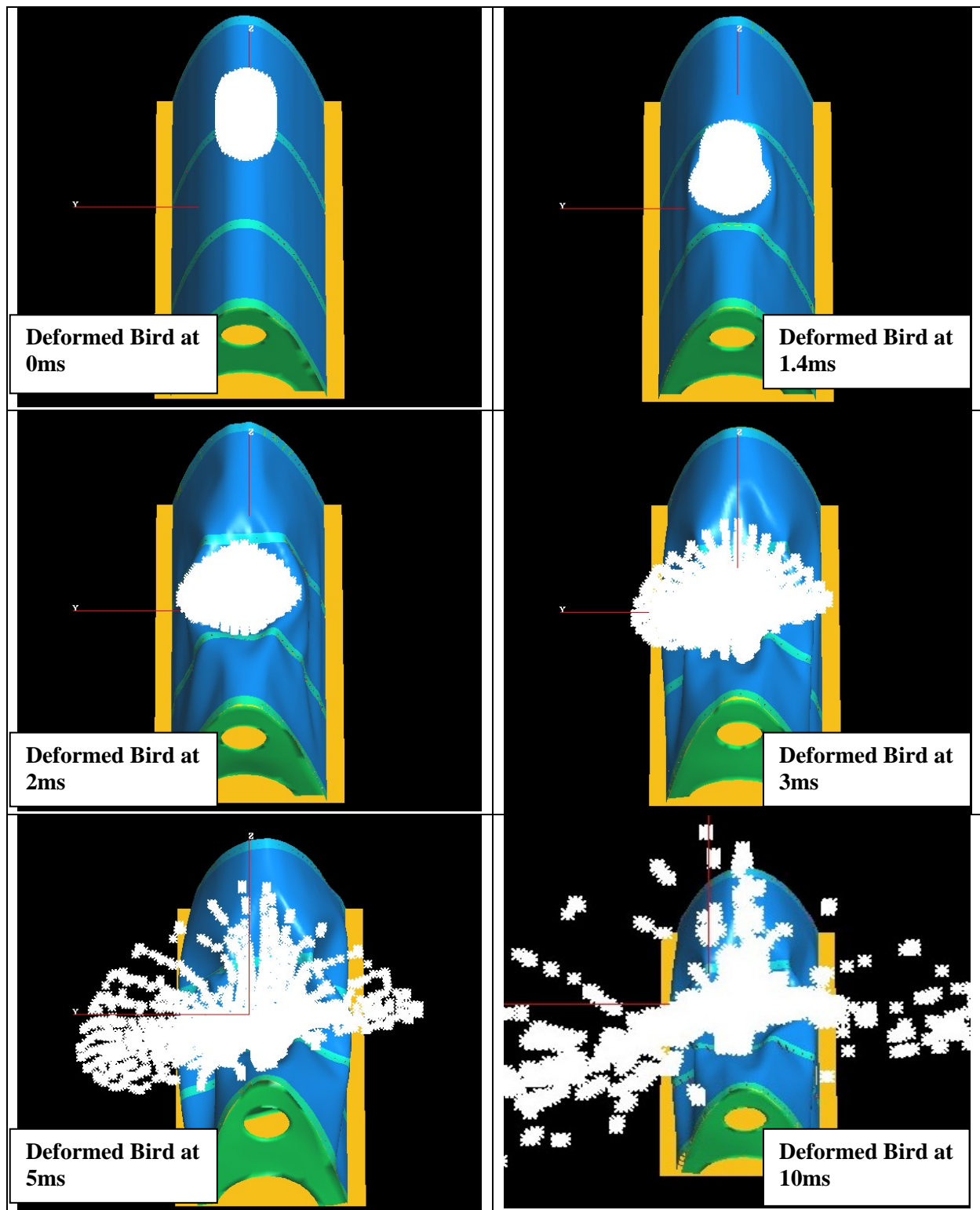


Fig. 4.19 Deformed shape of the Bird in FML5_Law1_1ms

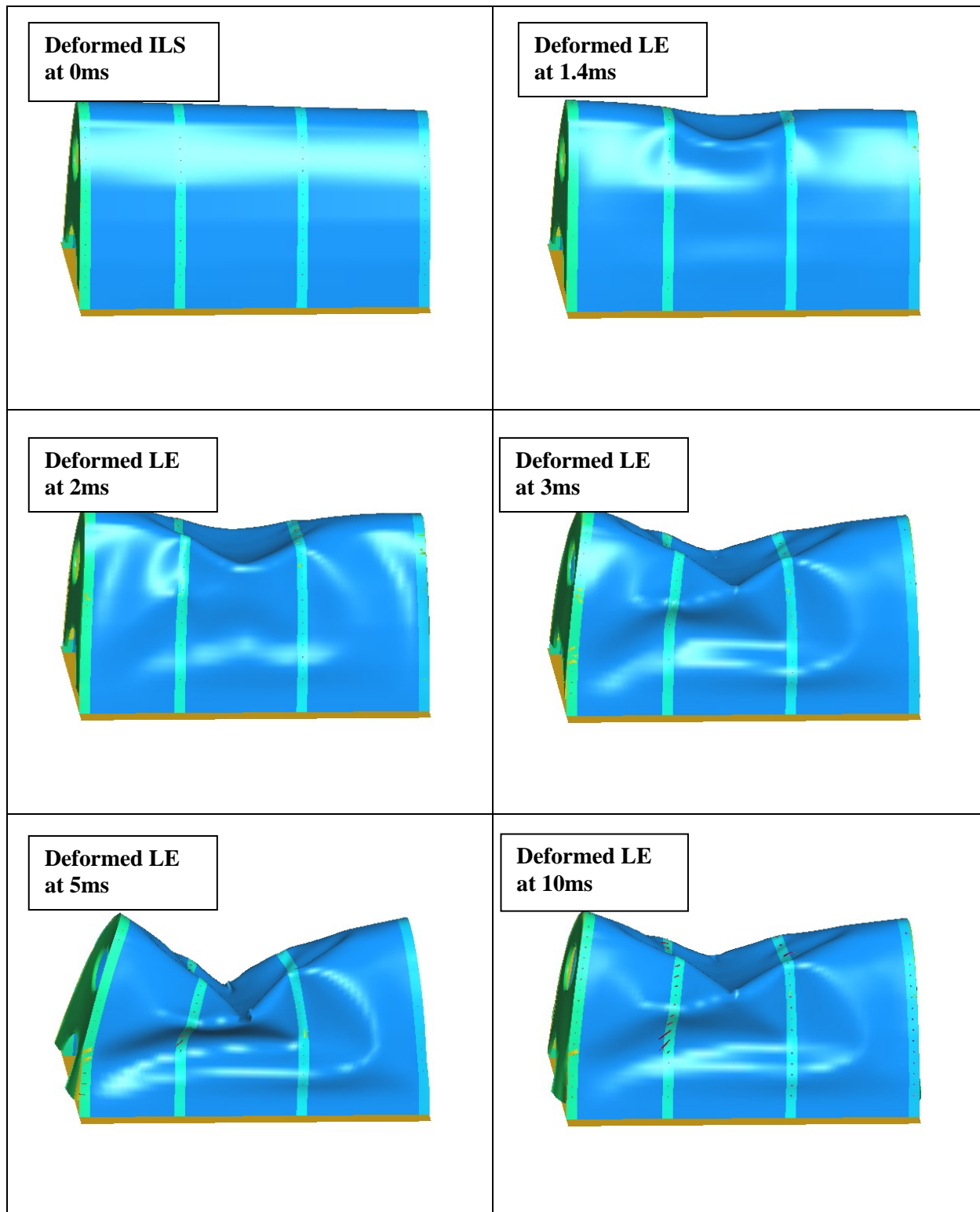
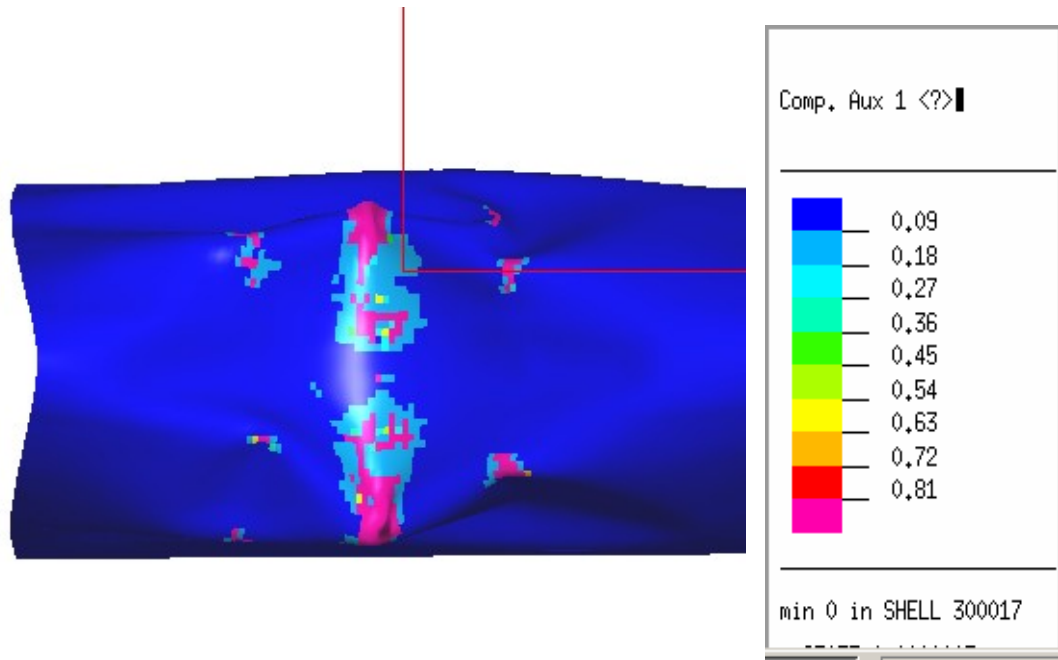
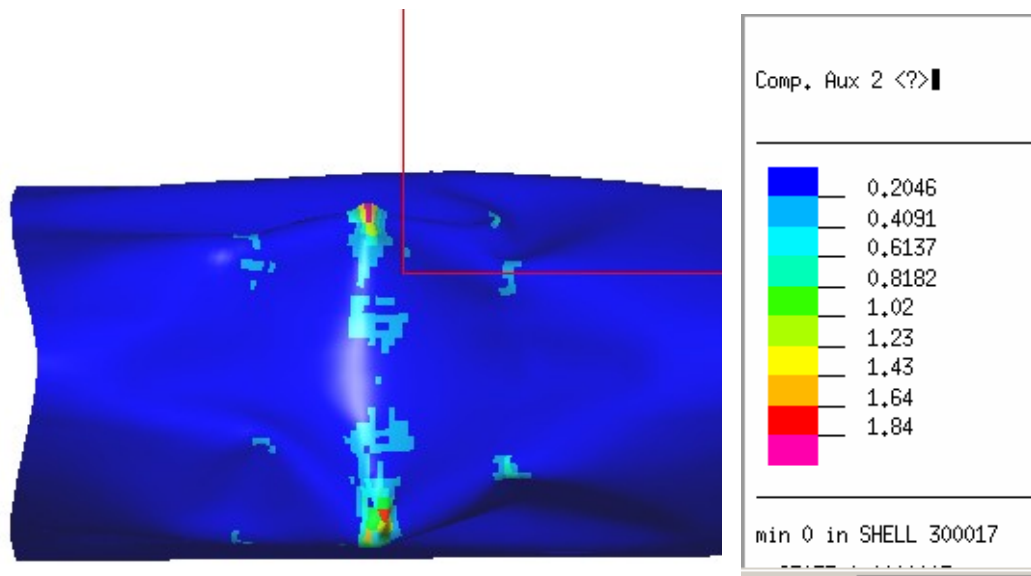


Fig. 4.20 Damaged states of the LE structure with FML5_Law1_1ms

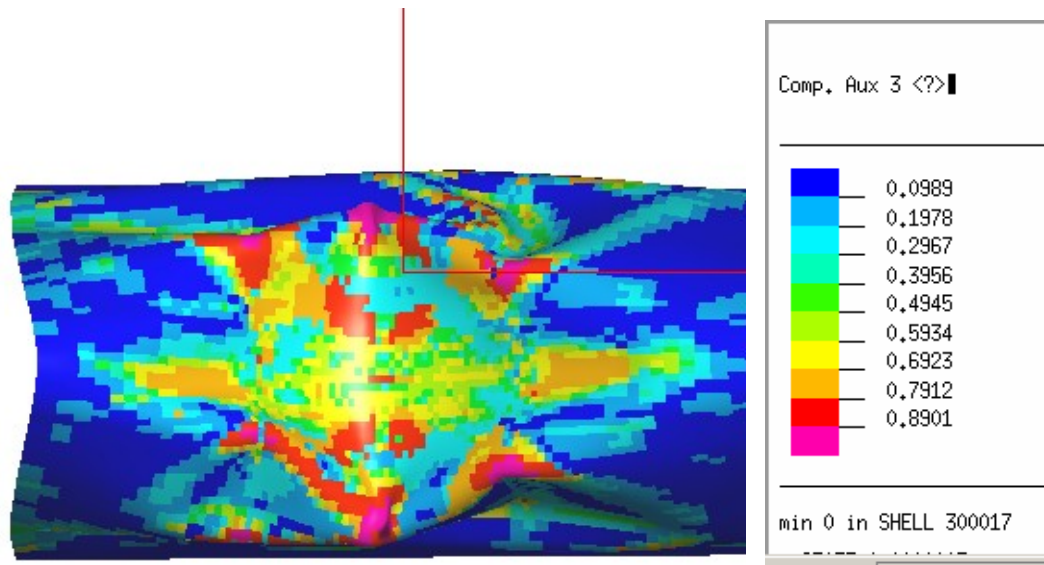


(a) Damage pattern

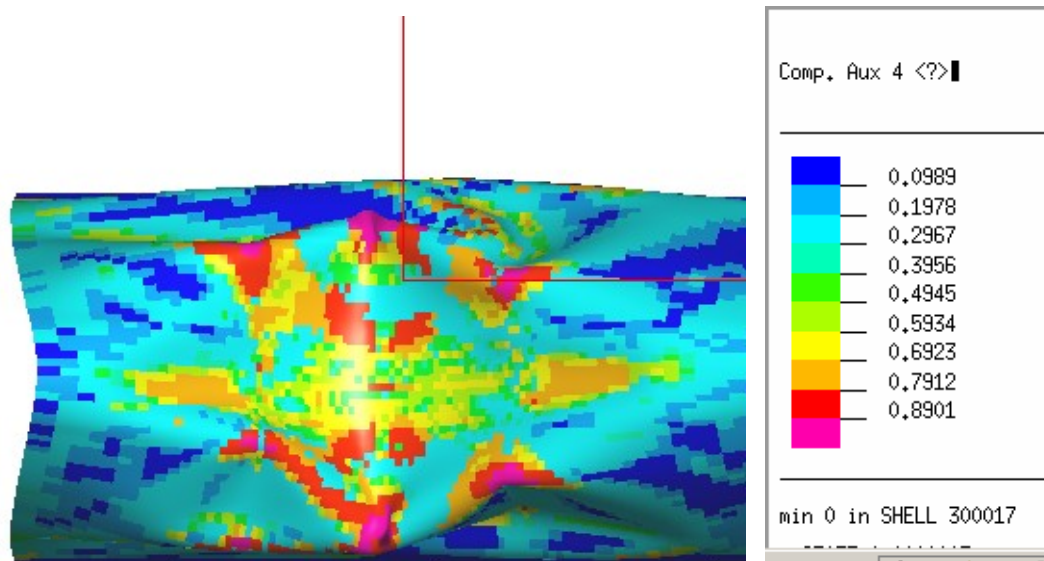


(b) Plastic strain pattern

**Fig. 4.21 Damage and plastic strain in the LE skin at the final state of FML5_Law1_1ms
(LAYER 1: Aluminium alloy)**

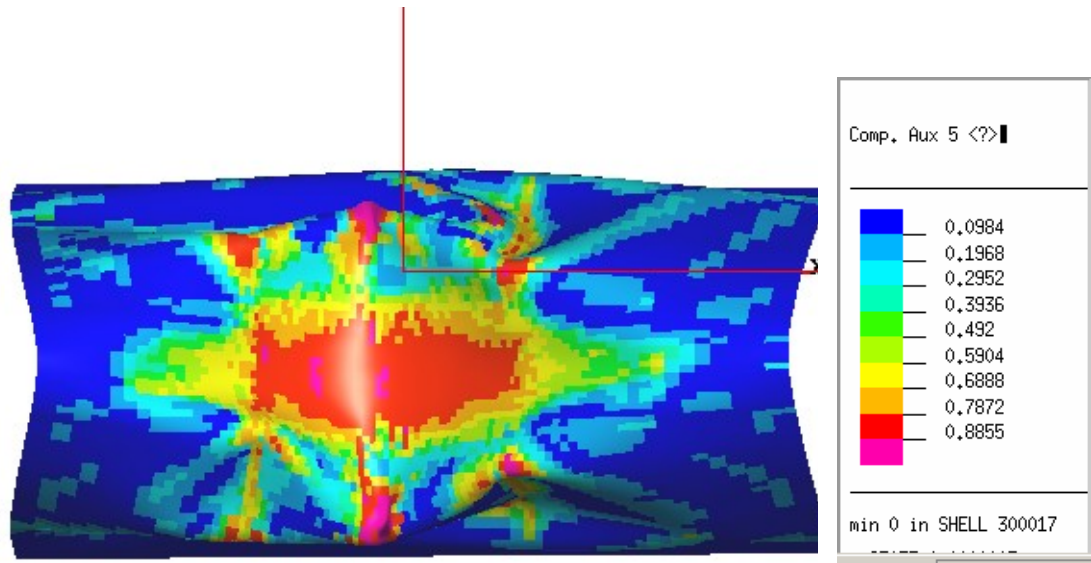


(a) Shear damage pattern

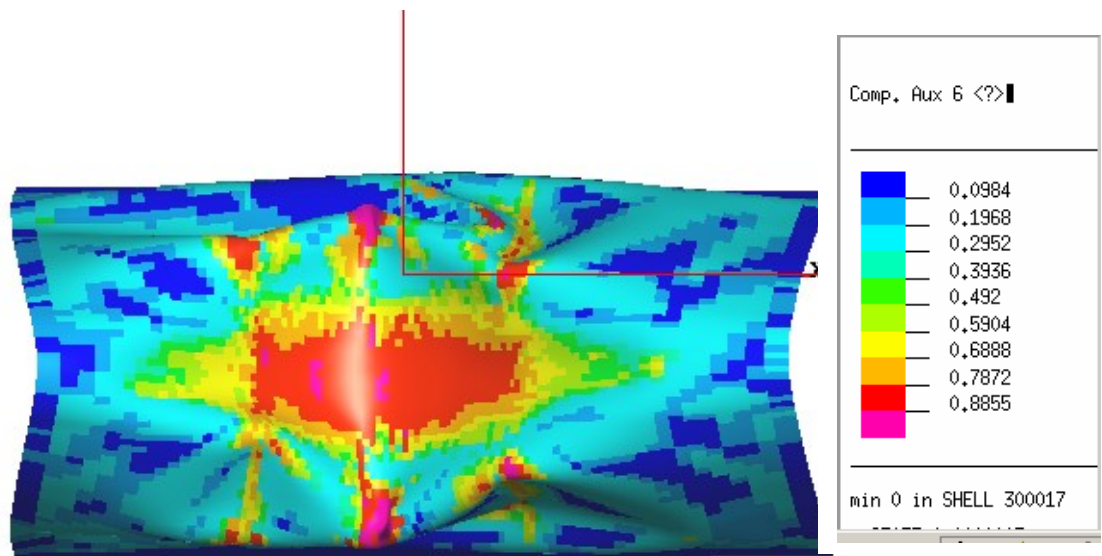


(b) Transverse damage pattern

**Fig. 4.22 Damage in the LE skin at the final state of FML5_Law1_1ms
(LAYER 2: 0 degree composite)**

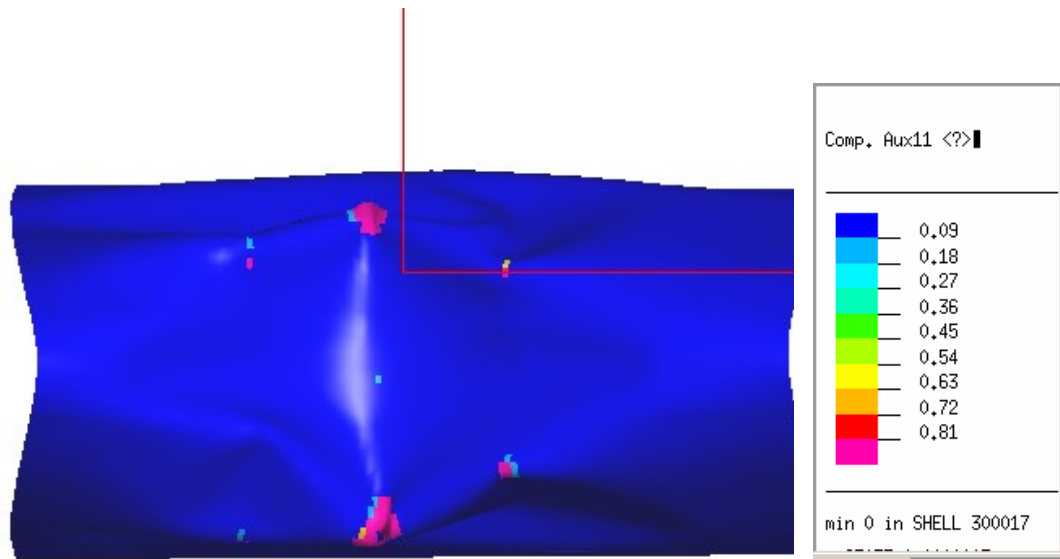


(a) Shear damage pattern

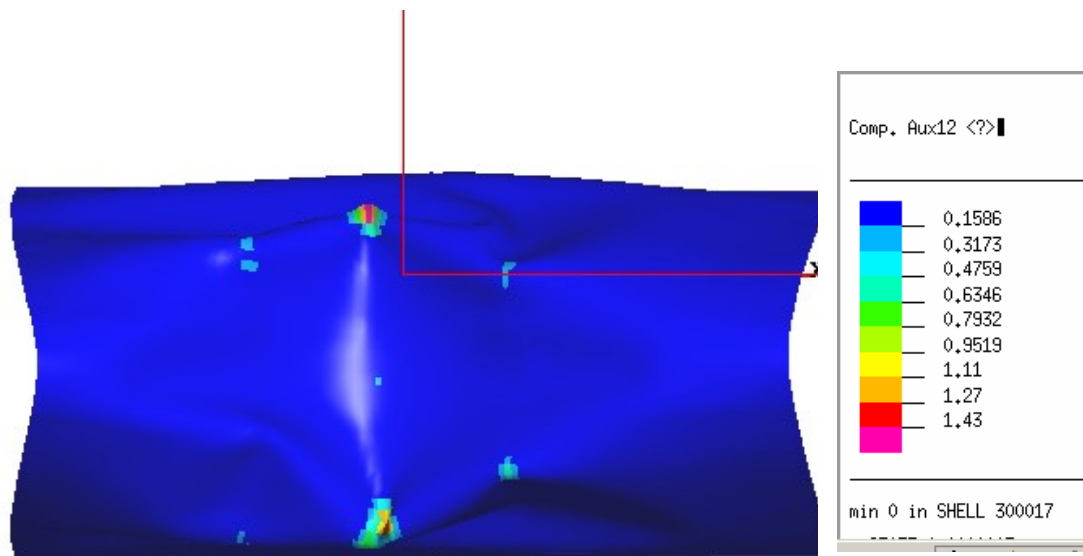


(b) Transverse damage pattern

**Fig. 4.23 Damage in the LE skin at the final state of FML5_Law1_1ms
(LAYER 3: 90 degree composite)**



(a) Damage pattern



(b) Plastic strain pattern

Fig. 4.24 Damage in the LE skin at the final state of FML5_Law1_1ms

(LAYER 6: aluminium alloy)

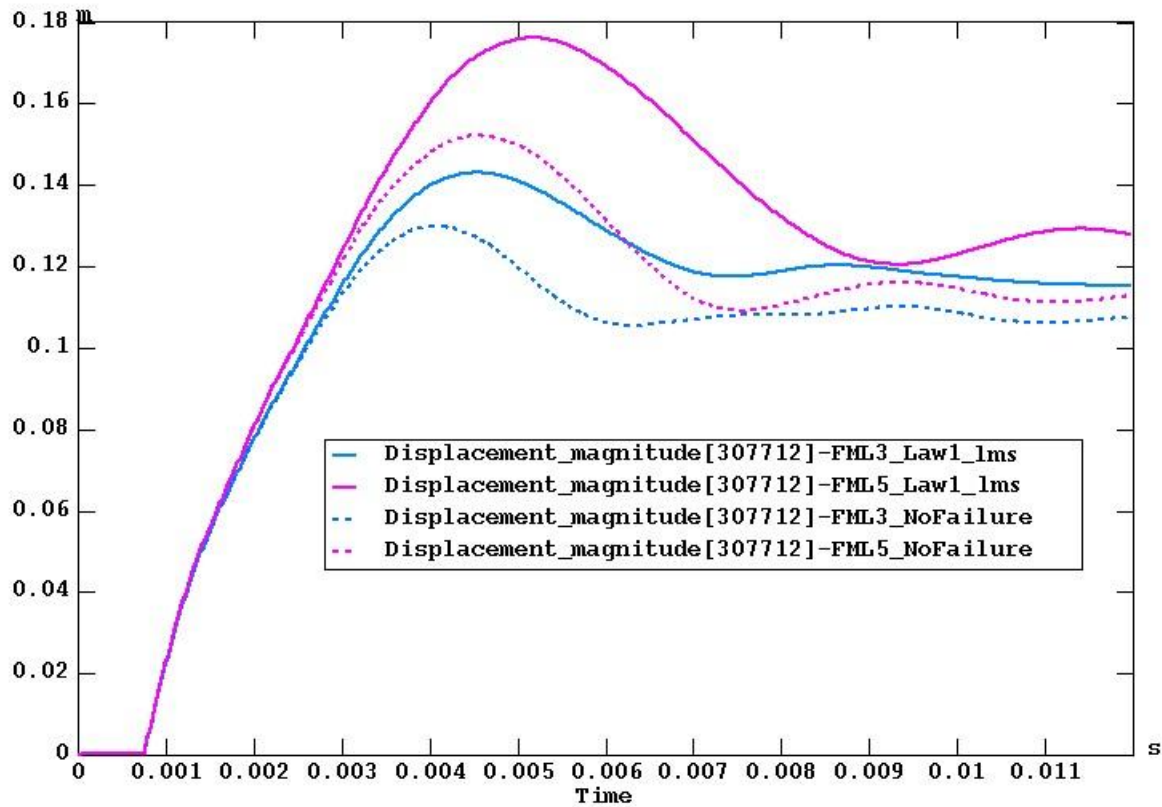


Fig. 4.25 Comparison of displacements of FML3 and FML5 skin glare lay-ups

Table 4.2 Summary results

Simulation Number	Simulation ID	Maximum Displacement (mm)	Residual Displacement (mm)	Number of failed Rivets
1	FML3_Law1_0ms	196	170	103
2	FML3_Law2_0ms	178	152	85
3	FML3_Law1_1ms	143	115	92
4	FML3_NoFailure	129	107	0
5	FML3_Law1_1ms_Bars	134	114	100
6	FML5_Law1_1ms	176	128	87
7	FML5_NoFailure	152	112	0



5 Conclusions

Pre-test simulations have been performed for two upcoming birdstrike tests on structures representative of a commuter wing leading edge. The skin is made from Glare, and preliminary calibrations for this material have been performed, based on experimental results from UOXF. The calibration takes into account the strain rate effects of Glare and uses the Ladeveze Global Ply composite model for the glass layers. The effects of different rivet failure laws have been investigated to try to generate a likely upper and lower bound on the behaviour of the real structure. The effects of using tension bars to stabilise the outer ribs have also been considered.

A number of inputs to the model were not available, particularly material properties of the glass layers in Glare and the failure strength of the rivets used in these structures. These values have had to be estimated.

The simulations predict that the bird will not penetrate the skin in either test. The FML5 lay-up is predicted to result in a greater skin deformation than the FML3 lay-up. Rivet failure is expected in the forward region of ribs 2 and 3 and possibly elsewhere also. Stabilising bars may not have much effect, since the rivets on the outer ribs may fail. The behaviour of the rivets will have a profound influence on the maximum deformation of the skin.

6 References

1. CRAHVI Deliverable D1.1.8 'High strain rate mechanical properties of Glare', Petrinic, N., Oxford University, September 2002.
2. CRAHVI Deliverable D1.4.2 'Report describing development of SPH/Lagrangian bird model', Jesús Ramos and Argiris Kamoulakos, ESI, July 2002.
3. CRAHVI Deliverable D2.1.3 'Geometry and FE model of two commuter leading edge structures', Melito V., Alenia, June 2002.
4. CRAHVI Deliverable D1.1.4 'Glare and composite plates. Basic background mechanical characteristics', Melito, V., Alenia, July 2002.
5. Vlot A. (1998), 'High strain rate test on Fibre Metal Laminates', Series 07, Delft university Press. The Netherlands.
6. Ladeveze P. and Le Dantec E. (1992), 'Damage modelling of the element ply for laminated composites', *Composites Science and technology*, **43**, pp. 257-267.
7. Soden, P.D., Hinton, M.J. and Kaddour A.S. (1998), 'Lamina properties, lay-up configurations and loading conditions for a range of fibre-reinforced composite laminates', *Composites Science and technology*, **58**, pp. 1011-1022.
8. CRAHVI Deliverable D1.2.1 'Review of composite failure models for impact simulation', Johnson A.F. November 2001.
9. Engineered materials handbook, Vol.1: Composites. Metals Park, Ohio, ASM International, 1987
10. Harris, C.E., Morris, D. H., 'A fractographic investigation of the influence of stacking sequence on the strength of notched laminated composites', *Fractography of Modern Engineering Materials: Composites and Metals*, ASTM STP 948, J.E. Masters and J.J. Au, Eds., American Society for Testing and Materials, Philadelphia, 1987, pp. 131-153.
11. PAM-CRASH Solver Reference Manual, Version 2002, (2002), ESI.



12. CRAHVI Deliverable D5.1.2 ‘Dynamic effects on riveted joint ARCAN test procedure’, Langrand B. and Fabis J., ONERA/DMSE/RCS, May 2002.
13. [Lee, H.T., Shaue, G.H., “The thermomechanical behaviour for aluminium alloy under uniaxial tensile loading”, Materials Science and Eng., A268, 1999, 154-164.](#)

